Journal of Energy Storage 134 (2025) 118114

Contents lists available at ScienceDirect

Journal of Energy Storage

journal homepage: www.elsevier.com/locate/est

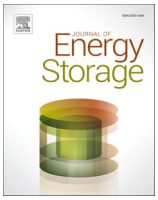

Research papers

Structural and electronic insights into $Na_{1-x}Li_xMgH_3$ hydrides for efficient solid-state hydrogen storage via lithium substitution

S. Saadoun [a,b], T. Ghellab [a,b,*], H. Baaziz [a,b,*], Z. Charifi [a,b]

[a] Department of Physics, Faculty of Science, University of M'sila, 28000 M'sila, Algeria
[b] Laboratory of physics and chemistry of materials, University of M'sila, Algeria

ARTICLE INFO

Keywords:
Hydrogen binding
$Na_{1-x}Li_xMgH_3$ alloys
Phase transition
Desorption temperature

ABSTRACT

This study investigates the hydrogen storage properties of $Na_{1-x}Li_xMgH_3$ hydrides (x = 0 to 1) using Density Functional Theory (DFT). Results show that lithium substitution enhances hydrogen storage, with gravimetric and volumetric capacities increasing from 6.00 wt% and 90 gH_2/l (x = 0) to 8.82 wt% and 214 gH_2/l (x = 1), surpassing U.S. DOE targets. The theoretical specific capacity improves from 1590 to 2331 mAh/g. A phase transition at x = 0.625 (from orthorhombic *Pnma* to trigonal *R3c*) improves hydrogen packing. Among dehydrogenation pathways, Pathway 7 shows the best practical potential, with desorption temperatures dropping from 256 K to 145 K as lithium content increases. Binding and cohesive energy analyses reveal enhanced stability and interactions due to lithium substitution. All compositions are wide-gap insulators, with band gaps increasing from ~3.45 eV to ~6.77 eV as lithium content rises. These findings position $Na_{1-x}Li_xMgH_3$ hydrides as promising candidates for solid-state hydrogen storage.

1. Introduction

Global warming presents a significant threat to humanity, necessitating a comprehensive understanding of its causes to develop effective mitigation strategies. Fossil fuels, which are responsible for approximately 75 % of global greenhouse gas emissions and nearly 90 % of carbon dioxide emissions, are the primary contributors to climate change [1].

The environmental impact of these emissions underscores the need to transition to sustainable energy sources. Advancements in clean, efficient, and renewable alternatives to fossil fuels are critical to ensuring a sustainable energy future. This shift not only mitigates climate change but also fosters energy independence and economic growth. By investing in renewable technologies, such as solar, wind, and hydroelectric power, we can build resilient infrastructure that supports both the environment and society [2]. In this context, renewable energy has emerged as a promising solution to address the global energy crisis [3], with many experts now considering hydrogen as a key energy carrier for the future. Due to its remarkable properties, hydrogen could play a central role in the transition to more sustainable and less polluting energy systems [4,5].

Hydrogen is widely regarded as one of the most promising alternative energy carriers, owing to its abundance, ease of production, exceptionally high energy density per unit mass, and environmentally benign combustion byproducts [6]. However, significant scientific and technological challenges remain, particularly in the areas of hydrogen production, distribution, storage, and utilization in fuel cells. Among these challenges, efficient hydrogen storage is a critical hurdle [7]. Current storage methods, such as compressed gas or cryogenic liquefaction, are costly and pose safety risks [8].

The solid-state storage of hydrogen is considered one of the most practical, efficient, and secure methods for hydrogen storage [9]. Consequently, research in this area is primarily focused on developing advanced materials with optimized properties, particularly those that are lightweight, chemically stable, non-toxic, and economically viable, while also ensuring long-term durability and high hydrogen storage capacity [10]. A recent study by Smruti et al. found a gravimetric hydrogen density of 6.36 wt% at 332.93 K for the yttrium-decorated azatriphenylene COF using VASP code [11]. Light chemical hydrides, such as $B_3N_3H_6$ (7.51 wt%), $C_3N_3H_6$ (7.19 wt%), and $Al_3N_3H_6$ (4.68 wt%), show high hydrogen storage capacities with branched hydrogen chains related to [XH_3NH_3] benzene structures [12]. Alkali metal tetrahydrides like $KAlH_4$ (5.7 wt%) [13], and $LiAlH_4$ (10.5 wt%) [14] are also noteworthy for their high storage capacity and excellent absorption

* Corresponding authors at: Department of Physics, Faculty of Science, University of M'sila, 28000 M'sila, Algeria.
E-mail addresses: torkia.ghellab@univ-msila.dz (T. Ghellab), hakim.baaziz@univ-msila.dz (H. Baaziz).

https://doi.org/10.1016/j.est.2025.118114
Received 9 June 2025; Received in revised form 1 August 2025; Accepted 15 August 2025

properties.

The development of safe, compact, and lightweight hydrogen storage materials is essential for future fuel cells and hydrogen combustion applications, especially with respect to the high hydrogen density offered by perovskite hydrides [15]. Metal hydrides, such as LiH and MgH_2, have attracted considerable attention due to their relatively high hydrogen densities (greater than 5 wt%) [16], However, these materials face challenges, including slow absorption kinetics, high thermal stability, and issues with the reversibility of the hydrogen absorption and desorption processes [17]. In recent years, ternary hydrides, particularly those containing magnesium and alkali metals, have been the focus of extensive research due to their potential advantages [18,19].

The ternary hydrides, such as those involving alkali elements like Li, are promising candidates for advanced hydrogen storage systems because of their cost-effectiveness and compactness. Key parameters for evaluating the performance of such materials include high volumetric and gravimetric hydrogen storage densities, fast absorption kinetics, favorable mechanical properties, and the ability to release hydrogen under normal conditions [5,20].

Among these, perovskite hydrides, represented by $AHgH_3$ (where A is an alkali metal such as Li, Na, or K), have garnered significant attention for their hydrogen storage potential. These materials are lightweight and can host multiple hydrogen atoms per metal atom, often as high as two in many cases [21]. For instance, $NaMgH_3$ exhibits a hydrogen content exceeding 6 wt% and a volumetric density of 88 kg/m^3 [22]. Additionally, cubic $AMMgH_3$ hydrides (where AM = Li, Na, K, and Rb) show promising hydrogen storage capacities. The calculated gravimetric hydrogen contents for $LiMgH_3$, $NaMgH_3$, $KMgH_3$, and $RbMgH_3$ are 8.76 wt%, 5.97 wt%, 4.52 wt%, and 2.68 wt%, respectively [23]. These materials have demonstrated promising potential for hydrogen storage applications, with notable reversibility in hydrogen absorption and desorption processes.

Recent research has focused on alloying magnesium with lithium (Li) to enhance the hydrogen storage characteristics of magnesium-based hydrides. Lithium, with its low atomic mass and high reactivity, has been found to reduce the thermal stability of Mg-based hydrides, lowering desorption temperatures and improving kinetic performance [24,25]. Li—Mg alloys have exhibited significant potential in overcoming the thermodynamic challenges associated with pure magnesium. The alloying of lithium with magnesium promotes phases that accelerate hydrogen absorption and release, attributed to improved diffusion rates and the catalytic action of lithium [26,27].

Catalysts play a key role in hydrogen storage in solid materials (such as metal hydrides, complexes, or nanostructured materials) as they improve kinetics and sometimes the reversible storage capacity. MXenes, a family of 2D materials, are promising electrocatalysts for hydrogen storage due to their large surface area and high conductivity. Yong P. and Jiahao G. studied transition metal (Ti, Zn, Ru)-doped V_2C MXene, finding a hydrogen dissociation energy of 1.646 eV and enhanced adsorption [28]. Borophene, another 2D material, shows potential for water splitting but suffers from low activity. To address this, Feihong et al. developed six Single Atom Catalysts (SACs) by combining borophene with transition metals (χ_3Pt, χ_3Co, χ_3Ni, β_{12}Pt, β_{12}Co, β_{12}Ni), improving hydrogen evolution reaction (HER) kinetics and thermodynamics [29,30].

Computational studies by Cheng et al. [31] have explored the thermodynamic stability of $LiMgH_3$ and Li_2MgH_4 at ambient temperatures using density functional theory (DFT). Experimental attempts by Ikeda et al. [32] to synthesize Li-Mg-H hydrides through mechanical milling of LiH and MgH_2 in hydrogen for 20 h yielded no evidence of the ternary hydride. However, subsequent computational models predicted that Li_2MgH_4 would adopt an orthorhombic structure (*Pbam* space group), while $LiMgH_3$ would adopt a trigonal structure (***R3c*** space group), akin to the $LiTaO_3$ structure type. The synthesis of MgH_2 and LiH was found to be neither stable nor energetically favorable [33– 35]. The substitution of Na with Li (Na = 22.99 u, Li = 6.94 u) alters the thermodynamic properties of the material, leading to a higher gravimetric hydrogen capacity, which is expected to enhance the hydrogen storage ability of the parent material. This substitution also results in a reduction of unit cell parameters, as noted by several authors [36,37].

Coronado et al. [38] prepared $Na_{1-x}Li_xMgH_3$ (x = 0, 0.25, 0.5, 0.75, 1) ternary hydrides using a high-pressure technique and found that the introduction of Li causes a decrease in unit cell parameters, an increase in the tilting angle, and more distortion of the MgH_6 octahedra due to the smaller ionic size of Li^+ compared to Na^+. Additionally, hydrogen desorption temperatures were found to decrease due to the reduced structural stability of the Li-containing perovskites.

In this study, we systematically investigate the impact of lithium substitution on the structural, thermodynamic, electronic, and hydrogen storage properties of $Na_{1-x}Li_xMgH_3$ (x = 0, 0.25, 0.50, 0.625, 0.75, and 1) hydrides using first-principles calculations. We evaluate the enhancement in hydrogen storage capacity, analyze the thermodynamic stability of various dehydrogenation pathways, and explore the evolution of electronic properties with increasing lithium content. Our findings reveal a promising combination of increased hydrogen storage capacity, lower desorption temperatures, and enhanced electronic stability, positioning $Na_{1-x}Li_xMgH_3$ as a potential candidate for next-generation solid-state hydrogen storage applications.

2. Details of computation

The FP-LAPW method [39,40], divides the computational cell into two distinct regions: the interstitial region and the spherical regions surrounding the atoms. In the spherical regions, the wavefunctions are expanded using spherical harmonics, while in the interstitial region, they are represented as plane waves [41]. This approach is implemented in the WIEN2k code [42], which was selected for the first-principles calculations carried out in this study.

For evaluating the exchange-correlation potential, we applied both the Local Density Approximation (LDA) and the Generalized Gradient Approximation (GGA), using the parametrization by Perdew, Burke, and Ernzerhof (PBE) [43]. Additionally, the Engel-Vosko (eV-GGA) method [44] and the modified Becke-Johnson exchange potential (mBJ) [45] were utilized to assess the electronic properties. The wavefunctions in the interstitial region were expanded in a plane-wave basis with a cutoff value of $k_{max} \times$ R.M.T. = 9, where R.M.T. represents the radius of the Muffin-Tin sphere and k_{max} denotes the maximum value of the plane wave vector. The charge density was expanded using Fourier analysis up to a maximum value of G_{max} = 12 $Ryd^{1/2}$. The valence wavefunctions inside the Muffin-Tin spheres were expanded up to l_{max} = 10. The energy difference between the core and valence states was set to −6.0 Ryd for the current calculations. A convergence criterion of 10^{-4} Ryd was used to achieve self-consistent total energy. A 9 × 9 × 9 k-point mesh was employed for sampling the first Brillouin zone (BZ). Finally, the total energy dependence on the cell volume was fitted to the Murnaghan equation of state (EOS) [46].

3. Results and discussion

To investigate the structural stability and alloy behavior of the $Na_{1-x}Li_xMgH_3$ (x = 0, 0.25, 0.50, 0.625, 0.75, and 1) system, we considered two prototype crystal structures commonly reported for related hydrides: the orthorhombic $GdFeO_3$-type structure (space group ***Pnma***, No. 62) [47] and the trigonal $LiTaO_3$-type structure (space group ***R3c***, No.161) [48]. These configurations serve as representative low-symmetry distortions of the ideal cubic perovskite, often stabilized in hydride perovskites depending on the chemical composition and external conditions.

The $NaMgH_3$ compound crystallizes in the orthorhombic ***Pnma*** structure, with a unit cell containing 20 atoms. The Na atoms occupy the 4c Wyckoff sites (x, ¼, z), Mg atoms are located at the 4b site (0, 0, ½), and hydrogen atoms are distributed over two sets of positions: 4c (x, ¼,

Table 1
Hydrogen gravimetric capacity ($C_{gwt\%}$), hydrogen volumetric capacity (ρ_{vol}), and theoretical specific capacity (Q_{th}) of $Na_{1-x}Li_xMgH_3$ ($x = 0$, 0.25, 0.5, 0.625, 0.75, 1) alloys.

Alloys	*H_2 gravimetric capacity ($Cg_{wt\%}$)*	*H_2 volumetric capacity (ρ_{vol}) ($g.H^2L^{-1}$)*	*Theoretical specific capacity (Q_{th}) (mAh g^{-1})*
x = 0	**6.00,** 6.00 [11]	**90,** 88 [11], 88.57 [8]	**1590,** 1598 [8]
x = 0.25	**6.52**	**92**	**1728**
x = 0.5	**7.14**	**98**	**1891**
x = 0.625	**7.50**	**196**	**1995**
x = 0.75	**7.89**	**204**	**2088**
x = 1	**8.82,** 8.82 [51]	**214**	**2331**

z) and 8d (*x*, *y*, *z*), consistent with earlier reports [22,49]. In contrast, $LiMgH_3$ adopts a more symmetric rhombohedral structure with the ***R3c*** space group. In this phase, the Li atoms reside on the 6a sites (0, 0, *z*), Mg atoms on the 6a site at the origin (0,0,0), and hydrogen atoms occupy the general 18b positions (*x*, *y*, *z*), as outlined by our fully relaxed structural parameters.

To model the mixed $Na_{1-x}Li_xMgH_3$ system across the compositional range (x = 0.00, 0.25, 0.50, 0.625, 0.75, and 1.00), we employed a substitutional approach within expanded supercells derived from the parent ***Pnma*** ($NaMgH_3$) and ***R3c*** ($LiMgH_3$) structures.

For $x = 0.25$ and 0.50, we constructed 2 × 2 × 1 supercells of the ***Pnma*** primitive unit cell (initially containing 4 Na, 4 Mg, and 12H atoms), yielding 16 alkali sites. Systematic replacement of Na with Li produced the alloy configurations: 4 Li + 12 Na ($x = 0.25$) and 8 Li + 8 Na ($x = 0.50$), with Mg and H counts scaled proportionally to 16 Mg and 48H to preserve stoichiometry. The $x = 0.625$ composition required a 1 × 2 × 1 supercell (8 alkali sites), resulting in a 5 Li + 3 Na distribution. For $x = 0.75$, we modeled the system using a primitive ***R3c***-derived cell (3 Li + 1 Na, 4 Mg, 12H). The end-members ($x = 0.00$ and 1.00) retained their pristine 20-atom unit cells. This strategy ensured chemically representative configurations while mitigating artificial ordering effects inherent to smaller supercells.

3.1. Hydrogen storage capacity

Meeting the stringent hydrogen storage standards set by the US Department of Energy (DOE) for 2025 is a significant challenge. The DOE requires gravimetric and volumetric storage densities to exceed 5.5 wt% and 40 gH_2/l, respectively [2,18,49]. Achieving these targets is crucial for fuel cells and other energy storage systems, as they need to store large amounts of hydrogen while maintaining a compact, lightweight structure. However, the low atomic mass of hydrogen is a fundamental challenge in achieving high gravimetric density.

Volumetric hydrogen storage density, expressed in grams of hydrogen per liter (gH_2/l), measures the amount of hydrogen stored per unit volume of the material. This metric is critical for applications where space is limited, such as in onboard vehicles or stationary storage systems [1,8]. A higher volumetric density allows more hydrogen to be stored in a compact space, enhancing the efficiency of hydrogen storage systems.

To evaluate the hydrogen storage potential of $Na_{1-x}Li_xMgH_3$ (x = 0, 0.25, 0.5, 0.625, 0.75, 1) alloys we calculated the gravimetric ($Cg_{wt\%}$), volumetric (ρ_{vol}), and theoretical specific (Q_{th}) hydrogen storage capacities. Gravimetric hydrogen storage density is calculated using the following formula [50]:

$$Cg_{wt\%} = \frac{3M_H}{(1\text{-}x)M_{Na} + xM_{Li} + M_{Mg} + 3M_H} \times 100 \quad (1)$$

The molar masses of Hydrogen (H), Lithium (Li), Sodium (Na), and Magnesium (Mg) are 1.007 g/mol, 6.941 g/mol, 22.989 g/mol, and 24.305 g/mol, respectively. In this context, *x* represents the composition of Lithium.

For volumetric hydrogen storage density, the following formula is used:

$$\rho_{vol} = \frac{N_H M_H}{V N_A} \quad (2)$$

where N_H is the atomic number of hydrogen absorbed per formula unit, N_A is Avogadro's constant, V is the volume of the absorbent, and M_H is the molar mass of hydrogen.

The theoretical specific capacity (Q_{th}) is calculated using:

$$Q_{th} = \frac{n \times F}{3600 \times M_W} \quad (3)$$

Where n is the number of hydrogen molecules absorbed per mole of material, F is the Faraday constant, and M_W is the molecular mass of the alloy [8]. Table 1 and Fig. 1 summarize the hydrogen storage capacities for $Na_{1-x}Li_xMgH_3$ alloys. The gravimetric hydrogen storage capacity increases from 6.00 wt% ($x = 0$) to 8.82 wt% ($x = 1$). This increase is attributed to the smaller atomic mass of lithium ($m_{Li} = 3$ g/mol) compared to sodium ($m_{Na} = 22.99$ g/mol), reducing the overall mass of the material and allowing for a higher hydrogen percentage by weight. These values exceed the DOE's gravimetric target of 5.5 wt%, indicating the potential of these compounds for hydrogen storage applications.

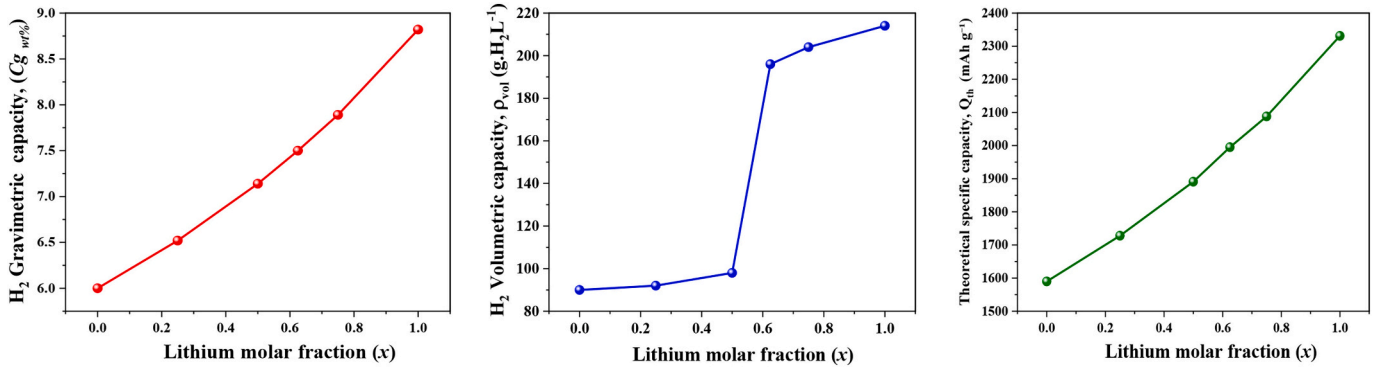

Fig. 1. Hydrogen gravimetric capacity ($Cg_{wt\%}$), hydrogen volumetric capacity (ρ_{vol}), and theoretical specific capacity (Q_{th}) of $Na_{1-x}Li_xMgH_3$ alloys (x = 0, 0.25, 0.5, 0.625, 0.75, 1) as a function of the lithium molar fraction (x).

Table 2
Equilibrium total energy values in Rydberg for $Na_{1-x}Li_xMgH_3$ ($x = 0, 0.25, 0.5, 0.625, 0.75, 1$) in the ***Pnma*** and ***R3c*** phases. The table also includes the total energies of the most stable phases of H_2 ($P2_12_12_1$), $L(Im\bar{3}m)$, $Na(Im\bar{3}m)$, Mg ($P6_3/mmc$), as well as LiH ($Fm\bar{3}m$)and NaH ($Fm\bar{3}m$). Additionally, the total energies of isolated H, Li, Na, and Mg atoms are presented using both GGA and LDA approximations.

Category	System	Total Energy (Ryd)			
		GGA		LDA	
Isolated Atoms	*H*	−0.9002		−0.8898	
	Li	−14.7754		−14.6706	
	Na	−323.9924		−323.3109	
	Mg	−399.6800		−398.9117	
Compounds	H_2 ($P2_12_12_1$)	−2.29		−2.27	
	Li (***$Im\bar{3}m$***)	−14.92		−14.82	
	LiH (***$Fm\bar{3}m$***)	−16.13		−16.03	
	Mg ($P6_3/mmc$)	−399.80		−399.04	
	Na (***$Im\bar{3}m$***)	−324.09		−323.41	
	NaH ($Fm\bar{3}m$)	−325.27		−324.59	
	$Na_{1-x}Li_xMgH_3$	Total Energy (Ryd)			
Alloys		*Pnma*		*R3c*	
		GGA	*LDA*	*GGA*	*LDA*
	$x = 0$	−727.3855	−725.9477	−727.3822	−725.9444
	$x = 0.25$	−650.0929	−648.8002	−650.0907	−648.7974
	$x = 0.5$	−572.8026	−571.6545	−572.8018	−571.6521
	$x = 0.625$	−534.1576	−533.0812	−534.1584	−533.0824
	$x = 0.75$	−495.5137	−494.5084	−495.5146	−494.5109
	$x = 0.875$	−456.8726	−455.9409	−456.8741	−455.9434
	$x = 1$	−418.2287	−417.3701	−418.2345	−417.3762

Compared to other compounds, $NaTcH_3$ (2.44 wt%), $NaRuH_3$ (2.38 wt%), and $NaRhH_3$ (2.35 wt%) [52] have lower capacities. $KTcH_3$, $KRuH_3$, and $KRhH_3$ are even lower (2.16 wt%, 2.11 wt%, and 2.08 wt%, respectively) [52]. $Na_{1-x}Li_xMgH_3$ alloys with lithium substitution outperform potassium-based hydrides in gravimetric hydrogen storage. Mg_2CoH_6 (5.32 wt%) [53] offers better capacity but still falls short of $Na_{1-x}Li_xMgH_3$ at 8.82 wt%. Other compounds like Ca_2CoH_6 (4.16 wt%), Ba_2CoH_6 (1.77 wt%) [53], and Sr_2CoH_6 (2.53 wt%) [53] have even lower capacities. Mg_2FeH_5 (4.60 wt%) [54] and potassium hydrides such as KSc_3H_8 (4.43 wt%) and KV_3H_8 (4.03 wt%) [55] also show lower capacities. K_2LiAlH_6 (5.12 wt%) [56] exceeds most potassium hydrides but is still lower than the optimal $Na_{1-x}Li_xMgH_3$.

For the volumetric hydrogen capacity, the computed values increase from 90 g.H_2/l at $x = 0$ to 214 g.H_2/l at $x = 1$. The increase in volumetric capacity with higher lithium content suggests that these materials are capable of storing more hydrogen in a compact space, far surpassing the DOE's volumetric target of 40 g.H_2/l. This makes the alloys suitable for applications requiring efficient space utilization, such as in vehicles or stationary storage systems. Comparing this to other compounds, $NaRuH_3$ has the highest volumetric density at 4.81 g/cm^3, followed by $NaRhH_3$ (4.74 g/cm^3) and $NaTcH_3$ (4.51 g/cm^3) [52]. $KRuH_3$ and $KRhH_3$ have densities of 4.66 g/cm^3 and 4.60 g/cm^3, respectively, while $KTcH_3$ is lower at 4.38 g/cm^3 [52]. These are significantly higher than Mg_2CoH_6 (2.78 g/cm^3) and Ca_2CoH_6 (2.76 g/cm^3) [53], with Ba_2CoH_6 (4.31 g/cm^3) and Sr_2CoH_6 (3.62 g/cm^3) offering slightly higher densities. Rb_2CaAlH_6 (2.60 g/cm^3), K_2CaAlH_6 (1.73 g/cm^3), and Cs_2CaAlH_6 (3.36 g/cm^3) [57] have much lower densities. Potassium hydrides like KSc_3H_8 (2.40 g/cm^3), KV_3H_8 (3.60 g/cm^3), and KCr_3H_8 (3.80 g/cm^3) [55] have intermediate densities, while Mg_2FeH_5 has a density of 2.80 g/cm^3 [54].

The theoretical specific capacity increases from 1590 mAh/g at $x = 0$ to 2331 mAh/g at $x = 1$, showing a clear trend that higher lithium content enhances the alloy's hydrogen storage capacity. The theoretical values suggest that the material's potential to store hydrogen increases significantly as the lithium concentration rises, aligning with the observed trends in gravimetric and volumetric capacities. A clear positive correlation between the lithium content (x) and all three capacities (gravimetric, volumetric, and theoretical specific) is evident. As lithium content increases, the lattice likely expands, creating larger interstitial sites that can accommodate more hydrogen atoms. This expansion may be responsible for the observed increase in volumetric capacity, indicating that higher lithium concentrations could lead to phase transitions or structural rearrangements that enhance hydrogen storage.

3.2. Formation energy

To determine the stability of a specific phase of $Na_{1-x}Li_xMgH_3$ ($x = 0$, 0.25, 0.5, 0.625, 0.75, and 1) alloys, the formation energy is one of the most crucial thermodynamic parameters in the study of hydrogen storage systems. It determines the enthalpy change during hydride formation and directly influences the reversibility and operating conditions of hydrogenation/dehydrogenation cycles. Xiao et al. [7] investigated four dehydrogenation pathways for select compositions ($x = 0$, 0.25, 0.5) using VASP with pseudopotential methods. Expanding on this, our study examines the full compositional range ($x = 0$, 0.25, 0.5, 0.625, 0.75, and 1) under both GGA and LDA. In this work, we analyzed four potential dehydrogenation mechanisms, selecting only those that release a practical amount of H_2 within a feasible temperature range. MgH_2 was deliberately excluded from the proposed reaction products due to its lower thermodynamic stability compared to LiH and NaH [33], ensuring the analysis focused on realistic and energetically favorable hydrogen release pathways.

The formation energies of the $Na_{1-x}Li_xMgH_3$ ($x = 0$, 0.25, 0.5, 0.625, 0.75, and 1) hydrides were calculated using the following reaction pathways:

$$Na_{1-x}Li_xMgH_3 \rightarrow xLi + (1-x)Na + Mg + \frac{3}{2}H_2 \quad (4)$$

$$Na_{1-x}Li_xMgH_3 \rightarrow xLiH + (1-x)Na + Mg + \left(\frac{3-x}{2}\right)H_2 \quad (5)$$

$$Na_{1-x}Li_xMgH_3 \rightarrow xLi + (1-x)NaH + Mg + \left(1+\frac{x}{2}\right)H_2 \quad (6)$$

$$Na_{1-x}Li_xMgH_3 \rightarrow xLiH + (1-x)NaH + Mg + H_2 \quad (7)$$

The hydride formation energies were calculated based on the following relation [21,58]:

$$\Delta H = \sum E_{Products} - \sum E_{Reactants} \quad (8)$$

Table 3
Formation enthalpies for the four pathways of $Na_{1-x}Li_xMgH_3$ ($x = 0$, 0.25, 0.5, 0.625, 0.75, 0.875, 1) calculated using GGA and LDA approximations for the ***Pnma*** and ***R3c*** structures.

Pathway 4	$Li_xNa_{1-x}MgH_3 \rightarrow xLi + (1-x)Na + Mg + \frac{3}{2}H_2$			
	ΔH (KJmol^{-1}.H$_2$)			
Alloys	*Pnma*		*R3c*	
	GGA	*LDA*	*GGA*	*LDA*
$x = 0$	−79.43	−121.69	−75.05	−117.35
$x = 0.25$	−79.29	−121.69	−76.36	−118.01
$x = 0.5$	−82.18	−123.98	−81.08	−120.90
$x = 0.625$	−83.82	−124.64	−84.82	−126.22
$x = 0.75$	−86.905	−125.89	−88.04	−129.17
$x = 0.875$	−93.65	−134.09	−95.58	−137.37
$x = 1$	−93.205	−137.96	−104.30	−145.97

Pathway 5	$Li_xNa_{1-x}MgH_3 \rightarrow xLiH + (1-x)Na + Mg + \left(\frac{3-x}{2}\right)H_2$			
	ΔH (KJmol^{-1}.H$_2$)			
Alloys	*Pnma*		*R3c*	
	GGA	*LDA*	*GGA*	*LDA*
$x = 0$	−79.42	−121.69	−75.09	−117.36
$x = 0.25$	−57.96	−97.08	−55.07	−93.40
$x = 0.5$	−39.51	−74.83	−38.46	−71.68
$x = 0.625$	−30.49	−63.11	−31.54	−64.69
$x = 0.75$	−22.91	−52.05	−24.09	−55.33
$x = 0.875$	−19.00	−47.95	−20.97	−51.23
$x = 1$	−7.88	−39.5137	−19.03	−47.52

Pathway 6	$Li_xNa_{1-x}MgH_3 \rightarrow xLi + (1-x)NaH + Mg + \left(1+\frac{x}{2}\right)H_2$			
	ΔH (KJmol^{-1}.H$_2$)			
Alloys	*Pnma*		*R3c*	
	GGA	*LDA*	*GGA*	*LDA*
$x = 0$	−33.48	−62.62	−29.14	−58.29
$x = 0.25$	−44.83	−77.39	−41.94	−73.71
$x = 0.5$	−59.20	−94.52	−58.15	−91.37
$x = 0.625$	−66.59	−102.49	−67.64	−104.07
$x = 0.75$	−75.42	−111.12	−76.60	−114.41
$x = 0.875$	−87.92	−126.71	−89.89	−129.99
$x = 1$	−93.20	−137.9699	−104.36	−145.98

Pathway 7	$Li_xNa_{1-x}MgH_3 \rightarrow xLiH + (1-x)NaH + Mg + H_2$			
	ΔH (KJmol^{-1}.H$_2$)			
Alloys	*Pnma*		*R3c*	
	GGA	*LDA*	*GGA*	*LDA*
$x = 0$	−33.46	−62.58	−29.13	−58.25
$x = 0.25$	−23.48	−52.74	−20.60	−49.07
$x = 0.5$	−16.53	−45.26	−15.48	−42.12
$x = 0.625$	−13.25	−40.93	−14.30	−42.51
$x = 0.75$	−11.41	−37.26	−12.60	−40.54
$x = 0.875$	−13.25	−40.54	−15.22	−43.82
$x = 1$	−7.87	−39.51	−19.02	−47.49

where E is the total energy of the bulk structures of the reactants and products.

Formation energy is defined as the energy required to form a compound from its constituent elements in their most stable states. Table 2 shows the ground-state structures and total energies E of LiH, NaH, Li, Na, and Mg, obtained through full geometry optimization. These structures belong to the space groups $Fm\bar{3}m$for LiH and NaH, $Im\bar{3}m$for Li and Na, and $P6_3/mmc$ for Mg [59]. We used a 2 × 2 × 2 supercell (16 atoms) for Li, Na, and Mg, and a unit cell with 8 atoms for LiH and NaH in total energy calculations. The equilibrium total energies of $Na_{1-x}Li_xMgH_3$ ($x = 0$, 0.25, 0.5, 0.625, 0.75, and 1) alloys in both ***Pnma*** and ***R3c*** phases are listed in Table 2 for both GGA and LDA approximations.

The four dehydrogenation paths (Eqs. 4–7) were employed to determine the formation enthalpy (ΔH) of $Na_{1-x}Li_xMgH_3$ ($x = 0$, 0.25, 0.5, 0.625, 0.75, and 1) alloys for both orthorhombic ***Pnma*** and trigonal ***R3c*** phases, as shown in Table 3. These data show that all reaction pathways are exothermic. Among all considered lithium compositions ($x = 0$ to 1), Pathway 4 (ΔH calculated from Eq. 4) consistently exhibits the lowest formation enthalpy (Fig. 2), indicating it is the most thermodynamically favorable route.

Across a broad range of lithium molar fractions ($x = 0$ to 0.75), both GGA and LDA calculations reveal that Pathway 4 consistently exhibits the most negative formation enthalpies, ranging from approximately −121.69 to −145.97 kJ mol^{-1} H_2 in the LDA approximation and − 79.43 to −104.30 kJ mol^{-1} H_2 in GGA. These values are notably lower often by 5 to 10 kJ mol^{-1} H_2 or more than those associated with the alternative pathways (Eq. 5, Eq. 6, and Eq. 7), particularly when compared to Eq. 5 and Eq. 7. This indicates that Pathway 4 represents a kinetically and thermodynamically preferred route for hydrogen release, likely facilitated by reduced lattice distortions and more favorable bond-breaking mechanisms during dehydriding. However, this tendency begins to shift at very high lithium content ($x \approx 0.875$–1.0), where Pathway 6 (Eq. 6) becomes increasingly competitive and even surpasses Pathway 4 in formation enthalpy under LDA, suggesting a possible change in thermodynamic preference at these higher doping levels.

Fig. 2 clearly indicates that the ***Pnma*** phase is the most stable for $x < 0.625$, having a lower ΔH, whereas for $x > 0.625$, the ***R3c*** phase becomes more stable due to its lower formation enthalpy. This passage marks a phase transition transformation from the orthorhombic ***Pnma*** to the trigonal ***R3c*** structure. For example, the formation enthalpy for $NaMgH_3$ ($x = 0$) is ΔH = −79.43 kJ mol^{-1} H_2 in the ***Pnma*** phase and ΔH = −75.05 kJ mol^{-1} H_2 in the ***R3c*** phase, indicating that ***Pnma*** is thermodynamically more stable at this composition. These results are in good agreement with earlier experimental and theoretical values, such as ΔH = −86.6 kJ mol^{-1} H_2 [34] and ΔH = −74.80 kJ mol^{-1} H_2 [6].

The GGA approximation yields better consistency with experimental data, likely due to its more accurate treatment of electron delocalization around H^- anions. In contrast, the LDA tends to overbind, resulting in an underestimation of the enthalpy by approximately 5–8 %. This finding aligns with prior studies on structural stability. Pan et al. observed negative formation enthalpy for Ta—C carbides, with higher carbon concentrations reducing stability [60]. Pan and Xu found Mo_2C MXene stable with negative ΔH related to chemical potential [61]. Alkali metal $AMAlH_4$ hydrides, particularly $KAlH_4$, showed stability due to Al—H and AM-H hybridization [62]. In TM-doped Pt_3Al, TM-Al sites were more stable than TM-Pt sites, with V and Nb doping stable, while Cu, Zn, Ag, and Pd doping were unstable [63]. In addition, Al-Zoubi et al. found $NaXH_3$ (X = Tc, Ru, Rh) hydrides stable, with $NaRhH_3$ being the most stable at $\Delta H_f = -1.07$ eV/atom [52]. Almahmoud et al. reported negative ΔH_f values for Y_2CoH_6 (Y = Ca, Ba, Mg, Sr), including Ba_2CoH_6 at −0.67 eV/atom [53]. For X_2FeH_5 hydrides, Ca_2FeH_5 had the highest stability at −0.272 eV/atom [54]. Obeidat et al. observed negative formation energies for KX_3H_8 (X = Sc, V, Cr), with KSc_3H_8 most stable at −10.14 eV/atom [55], and for $K_2BAl_{1-x}Ga_xH_6$ hydrides, K_2NaAlH_6 had a stability of 0.56 eV/atom [56]. Alkhalidi et al. confirmed stability for Rb_2CaAlH_6 (−0.69 eV/atom), K_2CaAlH_6 (−0.84 eV/atom), and Cs_2CaAlH_6 (−0.55 eV/atom) [57].

The observed phase transition between the orthorhombic ***Pnma*** and trigonal ***R3c*** structures at $x \approx 0.625$ can be physically attributed to the variation in ionic radius between Na^+ (1.02 Å) and Li^+ (0.76 Å). As lithium concentration increases, the smaller ionic radius of Li^+ induces a form of internal chemical pressure that contracts the lattice and increases internal strain. This strain likely destabilizes the ***Pnma*** phase in favor of the more compact and energetically favorable ***R3c*** structure at

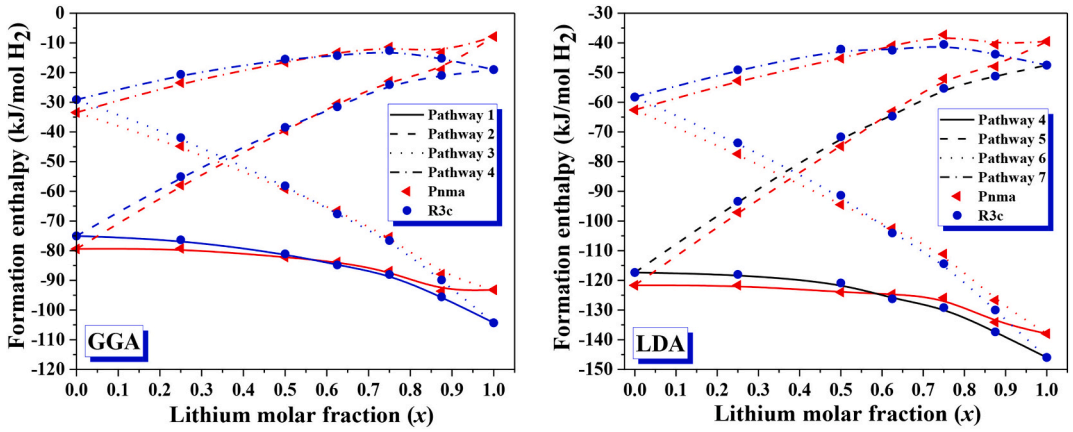

Fig. 2. Formation enthalpies for the four pathways of $Na_{1-x}Li_xMgH_3$ (x = 0, 0.25, 0.5, 0.625, 0.75, 0.875, 1) calculated using GGA and LDA approximations for the ***Pnma*** and ***R3c*** structures.

higher lithium contents. Moreover, this compositional tuning directly affects the electronic environment: Li, being more electronegative than Na, leads to stronger ionic Li—H bonds compared to Na—H, thereby enhancing the overall lattice cohesion in the ***R3c*** phase.

From a thermodynamic perspective, the exothermic nature of all four reaction pathways (Table 3) indicates that the formation of $Na_{1-x}Li_xMgH_3$ (x = 0, 0.25, 0.5, 0.625, 0.75, and 1) hydrides is spontaneous. However, the variation in the magnitude of the formation enthalpy (ΔH) with lithium concentration has direct implications for hydrogen release. Hydrides with more negative ΔH values (such as $x = 0$ and $x = 1$) possess stronger metal-hydrogen bonds, implying higher desorption temperatures and reduced reversibility.

Intermediate compositions, particularly x = 0.25 and 0.5, exhibit moderate formation enthalpies (ΔH ≈ −70 to −75 kJ mol^{-1}·H_2), suggesting a favorable balance between thermodynamic stability and hydrogen release conditions. Based on Van't Hoff analysis with an assumed entropy change of ΔS ≈ 130 J mol^{-1}·K^{-1} these values correspond to equilibrium H_2 pressures.

of ~1–10 bar near 100 °C. This makes them promising candidates for onboard hydrogen storage applications, where moderate operating temperatures are essential.

Our findings show that the ***Pnma*** phase is the most stable for $x <$ 0.625, while the ***R3c*** phase becomes energetically preferable beyond this composition. These trends support the idea of a composition-induced phase transformation that may be exploited to tune the thermodynamic and structural behavior of $Na_{1-x}Li_xMgH_3$ (x = 0, 0.25, 0.5, 0.625, 0.75, and 1) hydrides for hydrogen storage applications.

3.3. Desorption temperature

Reaction enthalpies (ΔH) are crucial thermodynamic parameters for evaluating and classifying hydrogen storage materials during both hydrogenation and dehydrogenation processes. These enthalpies govern the thermal characteristics of the hydriding reaction, directly influencing the operational temperatures required for hydrogen absorption and release [18]. A comprehensive understanding of these thermodynamic properties is pivotal for optimizing material performance in practical applications.

The desorption temperature (T_D) is a critical parameter when assessing the feasibility and safety of hydrogen storage materials [66] especially in applications such as fuel cells and energy storage systems. T_D determines the conditions under which hydrogen is released from the material. An optimal desorption temperature ensures efficient hydrogen release while minimizing the energy input. Moreover, an accurate understanding of the desorption temperature is essential for preventing unintended hydrogen leakage and designing safe, reliable storage systems [2,42].

In this study, the desorption temperature of $Na_{1-x}Li_xMgH_3$ (x = 0, 0.25, 0.5, 0.625, 0.75, and 1) alloys was determined using both GGA and LDA approximations. The thermodynamics of the dehydrogenation reaction are described by the Gibbs free energy Eq. [67]:

$$\Delta G = \Delta H - T\,\Delta S \tag{9}$$

For the vast majority of solid binary hydrides, the Gibbs free energy of the decomposition reaction (ΔG) becomes negative under dehydrogenation conditions, signaling a thermodynamically favorable process. The desorption temperature (T_D) can thus be precisely estimated by setting ΔG = 0, resulting in the simplified relation [50]:

$$T_D(K) = \frac{\Delta H}{\Delta S} \tag{10}$$

Where ΔH and ΔS represent the enthalpy and entropy changes of the dehydrogenation reaction, respectively, for $Na_{1-x}Li_xMgH_3$ (x = 0, 0.25, 0.5, 0.625, 0.75, and 1) alloys. This approximation is widely applicable to simple metal hydride systems, as demonstrated in prior studies [22,68].

Thermodynamic studies by Züttel [69] quantitatively show that the entropy change (ΔS) during metal hydride decomposition is approximately equivalent to the standard molar entropy of gaseous H_2, with ΔS ≈ $S(H_2)$ = 130.7 J mol^{-1} K^{-1} under standard conditions (300 K, 1 bar). This correspondence arises because the reaction entropy is primarily dominated by the configurational entropy gain when hydrogen transitions from the constrained solid-state environment to the three degrees of freedom in an ideal diatomic gas. The value of $S(H_2)$ is well-established through statistical mechanical calculations and spectroscopic data.

The desorption temperatures (T_D) for $Na_{1-x}Li_xMgH_3$ alloys, calculated using both GGA and LDA approximations, are presented in Table 4. For the parent compound $NaMgH_3$ (x = 0), previous experimental studies report reversible hydrogen desorption near 673 K [49,70] d Wei [17] suggesting a slightly lower onset at 623 K. Our GGA-based calculation yields a T_D of 607 K, which aligns well with these experimental values and the reported 638 K [20], confirming the compound's potential for reversible hydriding/dehydriding at moderate temperatures. When compared to other hydrides, $KTcH_3$ has the lowest desorption temperature (365 K), while $NaRhH_3$ has the highest (790 K), with $KTcH_3$ falling within the practical range (289–393 K) [52]. Ca_2CoH_6 desorbs at 376.51 K, while Ba_2CoH_6 reaches 492.14 K, and Mg_2CoH_6 has the lowest at 245.12 K [53]. X_2FeH_5 hydrides show even more variation: Mg_2FeH_5 desorbs at 240 K, and Ca_2FeH_5 at 460 K [54]. Lastly, K_2NaAlH_6 reaches a high of 413.4 K, while K_2LiGaH_6 has a low desorption temperature of 191.9 K, indicating tunable hydrogen release properties [56].

Table 4
Calculated total energies in the most stable phase for $Na_{1-x}Li_xMgH_3$ (x = 0, 0.25, 0.5, 0.625, 0.75, 1), along with the enthalpies of formation (ΔH) and desorption temperatures (T_D) based on reaction Pathways 4–7, using both GGA and LDA approximations.

Alloys	*Pathway 4*							
	Total energy (Ryd)		*ΔH (KJ mol^{-1}.H$_2$)*			*T_D (K)*		
			This work		*Expt. Data*	*This work*		*Expt. data*
	GGA	*LDA*	*GGA*	*LDA*		*GGA*	*LDA*	
$NaMgH_3$ (Pnma)	−727.3855	−725.9477	−79.43 −79.86 [33] −72.82 [8] - 86.6 [64]	−121.69	−74.80 [20] −96.7 [22] −98 [65]	607 623 [17] 673 [65]	931	638 [20] 659 [38]
$Li_{0.25}Na_{0.75}MgH_3$ (Pnma)	−650.0929	−648.8002	−79.29	−121.69		608	931	x = 0.2: 670 [38]
$Li_{0.5}Na_{0.5}MgH_3$ (Pnma)	−572.8026	−571.6545	−82.18	−123.98		628	948	684 [38]
$Li_{0.625}Na_{0.375}MgH_3$ (R3c)	−534.1584	−533.0824	−84.82	−126.22		648	965	
$Li_{0.75}Na_{0.25}MgH_3$ (R3c)	−495.5146	−494.5109	−88.04	−129.17		687	988	x = 0.8: 681 [38]
$LiMgH_3$ (R3c)	−418.2345	−417.3762	−104.30 −98.33 [33]	−145.97		799	1116	
Pathway 5								
$NaMgH_3$ (Pnma)	−727.3855	−725.9477	−79,42	−121,69		607	931	
$Li_{0.25}Na_{0.75}MgH_3$ (Pnma)	−650.0929	−648.8002	−57,96	−97,08		443	742	
$Li_{0.5}Na_{0.5}MgH_3$ (Pnma)	−572.8026	−571.6545	−39,51	−74,83		302	572	
$Li_{0.625}Na_{0.375}MgH_3$ (R3c)	−534.1584	−533.0824	−31,54	−64,69		241	494	
$Li_{0.75}Na_{0.25}MgH_3$ (R3c)	−495.5146	−494.5109	−24,09	−55,33		184	423	
$LiMgH_3$ (R3c)	−418.2345	−417.3762	−19,03 −59.75 [33]	−47,52		145	363	
Pathway 6								
$NaMgH_3$ (Pnma)	−727.3855	−725.9477	−33,48 −74.80 [33]	−62,62		256	479	
$Li_{0.25}Na_{0.75}MgH_3$ (Pnma)	−650.0929	−648.8002	−44,83	−77,39		342	592	
$Li_{0.5}Na_{0.5}MgH_3$ (Pnma)	−572.8026	−571.6545	−59,2	−94,52		452	723	
$Li_{0.625}Na_{0.375}MgH_3$ (R3c)	−534.1584	−533.0824	−67,64	−104,07		517	796	
$Li_{0.75}Na_{0.25}MgH_3$ (R3c)	−495.5146	−494.5109	−76,6	−114,41		586	875	
$LiMgH_3$ (R3c)	−418.2345	−417.3762	−104,36 −98.33 [33]	−145,98		798	1116	
Pathway 7								
$NaMgH_3$ (Pnma)	−727.3855	−725.9477	−33,46	−62,58 −74.80 [33]		256	478	
$Li_{0.25}Na_{0.75}MgH_3$ (Pnma)	−650.0929	−648.8002	−23,48	−52,74		179	403	
$Li_{0.5}Na_{0.5}MgH_3$ (Pnma)	−572.8026	−571.6545	−16,53	−45,26		126	346	
$Li_{0.625}Na_{0.375}MgH_3$ (R3c)	−534.1584	−533.0824	−14,3	−42,51		109	325	
$Li_{0.75}Na_{0.25}MgH_3$ (R3c)	−495.5146	−494.5109	−12,6	−40,54		96	310	
$LiMgH_3$ (R3c)	−418.2345	−417.3762	−19,02 −59.75 [33]	−47,49		145	363	

Fig. 3 illustrates the variation of desorption temperature as a function of lithium molar fraction (x) across the four proposed decomposition pathways. For Pathways 4 and 6, T_D increases steadily with rising Li content, indicating enhanced thermal stability. This trend correlates with the increasingly negative formation enthalpies observed upon Li substitution (Table 4). Notably, in Pathway 4, T_D remains relatively constant for $x < 0.625$ but rises significantly beyond this threshold, marking a critical point where lithium begins to substantially influence the compound's structural or electronic characteristics. This behavior is attributed to a composition-induced phase transition from the orthorhombic ***Pnma*** to the more stable trigonal ***R3c*** structure. The transition contributes to thermal stabilization by strengthening Li—H bonding and enhancing lattice cohesion. In contrast, for Pathways 5 and 7, desorption temperatures decrease with increasing lithium content, emphasizing the pathway dependent nature of desorption behavior. These differences underscore how structural and energetic factors jointly govern hydrogen

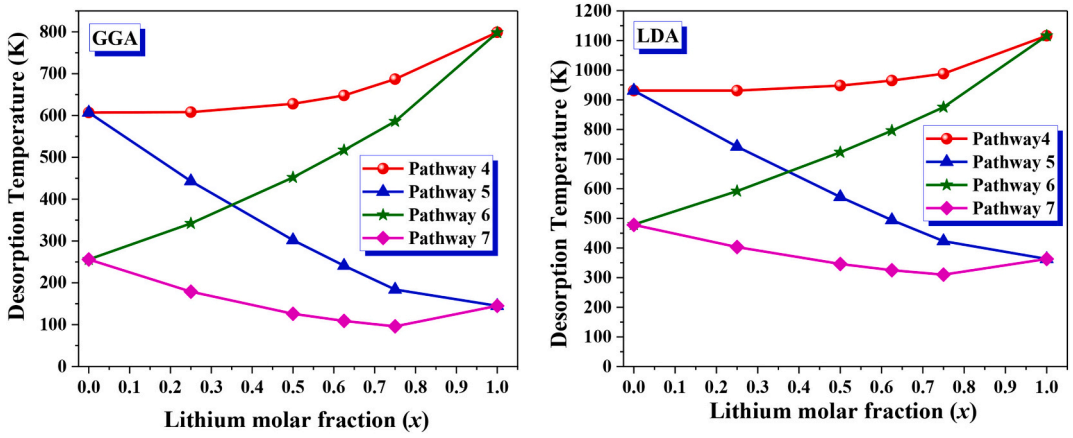

Fig. 3. The desorption temperature of $Na_{1-x}Li_xMgH_3$ (x = 0, 0.25, 0.5, 0.625, 0.75, 1) alloys for the four pathways as a function of lithium molar fraction (x), calculated using GGA and LDA approximations.

release properties. At all lithium concentrations (x = 0, 0.25, 0.5, 0.625, 0.75, 1), LDA calculations predict higher T_D values than GGA, reflecting LDA's known overbinding tendency. Despite this quantitative disparity, both methods reveal consistent qualitative trends, lending confidence to the overall conclusions.

Vasquez et al. [38] and Xiao's group [7] have emphasized that for optimal hydrogen storage performance, the decomposition enthalpy (ΔH) should fall within the range of 30–60 kJ mol^{-1} H_2, corresponding to desorption temperatures between 323 and 423 K (50–150 °C). They also reported that the entropy change (ΔS) typically lies between 95 and 140 J mol^{-1} K. If ΔH exceeds 60 kJ mol^{-1} H_2, higher desorption temperatures are needed to generate sufficient hydrogen pressure. Conversely, values below 30 kJ mol^{-1} H_2 may raise concerns about reversibility during hydrogen cycling [58]. Our results are consistent with these trends.

For decomposition path 4, we obtained ΔH values ranging from 79.43 to 104.30 kJ mol^{-1} H_2, requiring higher desorption temperatures (607–799 K), which aligns with the need for elevated thermal input when ΔH exceeds 60 kJ mol^{-1} H_2. In contrast, for paths 5 and 7, ΔH decreases significantly from 79.42 to 19.03 kJ mol^{-1} H_2 (path 5), and from 33.46 to 19.02 kJ mol^{-1} H_2 (path 7) as the lithium content increases. This results in reduced decomposition temperatures, from 607 K to 145 K (path 5) and 256 K to 145 K (path 7), indicating that these pathways are more thermodynamically favorable for hydrogen release. Among them, path 4 exhibits the lowest calculated energy, suggesting it is the most rational pathway. These findings are in good agreement with the conclusions of Xiao et al. [7], who reported that substituting Na with Li in perovskite-type $NaMgH_3$ could reduce the dehydrogenation enthalpy and enhance the thermodynamic performance. As illustrated in Fig. 3, the decomposition reaction enthalpies of $Na_{1-x}Li_xMgH_3$ (x = 0, 0.25, 0.5, 0.625, 0.75, and 1) exhibit different trend depending on the reaction pathway.

Along pathways 4 and 6, the enthalpy values slightly increase with rising lithium content, indicating that the dehydrogenation temperature tends to increase as more Li is incorporated. In contrast, for pathways 5 and 7, the enthalpies decrease significantly with increasing Li concentration, suggesting a reduction in the dehydrogenation temperature. This trend highlights that reactions following pathways 5 and 7 are thermodynamically more favorable for hydrogen release. The near-linear decrease in enthalpy observed for reactions (5) and (7) with increasing Li substitution from x = 0 to x = 1 suggests that substituting Li for Na in $NaMgH_3$ beneficially alters the thermodynamic properties. Notably, the reaction products of pathways (2) and (4) include LiH, which appears to contribute to the linear reduction in enthalpy. Compared to other alkali hydrides, LiH possesses a higher heat of formation 1390.81 k and greater cohesive energy −181.78 kJ/Mol.H_2 [50] implying stronger Li—H bonding. This robust interaction may facilitate the release of additional hydrogen atoms in the $Na_{1-x}Li_xMgH_3$ system.

These findings demonstrate that Li substitution plays a crucial role in modulating the thermodynamics of the dehydrogenation process. Understanding this effect deepens insight into the mechanism of Li incorporation in $NaMgH_3$. Furthermore, the favorable thermodynamic adjustment through Li doping could lead to enhanced hydrogen storage capacity, addressing a key criterion for the development of efficient hydrogen storage materials.

Although all four dehydrogenation pathways were investigated in terms of formation enthalpy and desorption temperature, a comparison between Pathway 4 and Pathway 7 highlights a clear trade-off between thermodynamic stability and hydrogen release efficiency. Pathway 4 consistently exhibits the lowest formation enthalpy across all compositions and structural phases, indicating a strong thermodynamic driving force for compound stability. However, this enhanced stability corresponds to high dehydrogenation enthalpies (−79.43 to −104.30 kJ mol^{-1} H_2), resulting in elevated desorption temperatures (607–799 K), which are less desirable for practical hydrogen storage systems operating at moderate temperatures. In contrast, Pathway 7, although slightly less favorable in terms of formation energy, demonstrates significantly lower dehydrogenation enthalpies (down to −19.02 kJ kJ mol^{-1} H_2) and much lower desorption temperatures (as low as 145 K), particularly in Li-rich compositions.

To address the high desorption temperatures, we propose applying strategies such as nanoscale engineering, doping with catalytic additives, and structural modifications across all pathways. Nanoscale engineering can enhance the surface area, while catalytic doping (e.g., Pd or Pt) and structural modifications can reduce activation energy and optimize thermodynamic properties, making these pathways more suitable for practical hydrogen storage at moderate temperatures.

These characteristics, combined with a structural phase transition to the more stable ***R3c*** phase beyond x = 0.625, make Pathway 7 more aligned with experimental observations and far more suitable for practical hydrogen storage applications. Therefore, while Pathway 4 represents a thermodynamically robust route, Pathway 7 emerges as the more convenient and efficient pathway for real-world implementation.

3.4. Hydrogen binding energy of $Na_{1-x}Li_xMgH_3$ alloys

The study focuses on the hydrogen binding energy of $Na_{1-x}Li_xMgH_3$ hydrides with varying lithium concentrations (x = 0, 0.25, 0.5, 0.625, 0.75, 1) across different hydrogen desorption stages (σ = 1, 2, 3), with hydrogen vacancy binding energy calculated using the formula presented in Eq. (11) [70].

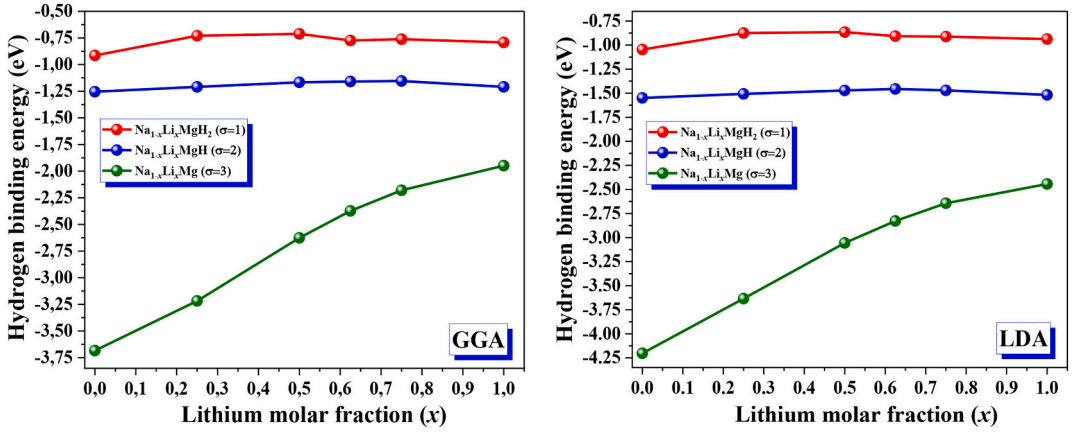

Fig. 4. Hydrogen binding energy of $Na_{1-x}Li_xMgH_2$ (σ = 1), $Na_{1-x}Li_xMgH$ (σ = 2), and $Na_{1-x}Li_xMg$ (σ = 3) as a function of lithium composition (x = 0, 0.25, 0.5, 0.625, 0.75, 1) using GGA and LDA approximations.

Table 5
Total and binding energy of $Na_{1-x}Li_xMgH_3$ (x = 0, 0.25, 0.5, 0.625, 0.75, 1) as a function of lithium composition across different hydrogen desorption stages (σ = 1, 2, 3) using GGA and LDA functionals.

Eq. 1 (σ = 1)	$E_{Bind} = E_{Na_{1-x}Li_xMgH_3} - E_{Na_{1-x}Li_xMgH_2} - \frac{1}{2}E_{H_2}$			
	Total energy (Ryd)		*Binding energy* (eV)	
Alloys	*GGA*	*LDA*	*GGA*	*LDA*
$NaMgH_2$ *(Pnma)*	−726.1733	−724.7358	−0.9143	−1.0463
$Li_{0.25}Na_{0.75}MgH_2$ *(Pnma)*	−648.8943	−647.6009	−0.7292	−0.8748
$Li_{0.5}Na_{0.5}MgH_2$ *(Pnma)*	−571.6053	−570.4559	−0.7115	−0.8653
$Li_{0.625}Na_{0.375}MgH_2$ *(R3c)*	−532.9565	−531.88066	−0.7741	−0.9080
$Li_{0.75}Na_{0.25}MgH_2$ *(R3c)*	−494.3136	−493.3088	−0.7619	−0.9129
$LiMgH_2$ *(R3c)*	−417.0313	−416.1723	−0.7918	−0.9374
Eq. 2 (σ = 2)	$E_{Bind} = E_{Na_{1-x}Li_xMgH_3} - E_{Na_{1-x}Li_xMgH} - E_{H_2}$			
NaMgH (Pnma)	−725.0033	−723.5638	−1.2544	−1.5497
$Li_{0.25}Na_{0.75}MgH$ *(Pnma)*	−647.7140	−646.4194	−1.2095	−1.5075
$Li_{0.5}Na_{0.5}MgH$ *(Pnma)*	−570.4269	−569.2763	−1.1660	−1.4721
$Li_{0.625}Na_{0.375}MgH$ *(R3c)*	−531.7832	−530.7054	−1.1592	−1.4558
$Li_{0.75}Na_{0.25}MgH$ *(R3c)*	−493.1398	−492.1328	−1.1537	−1.4708
LiMgH (R3c)	−415.8556	−414.9946	−1.2095	−1.5184
Eq. 3 (σ = 3)	$E_{Bind} = E_{Na_{1-x}Li_xMgH_3} - E_{Na_{1-x}Li_xMg} - \frac{3}{2}E_{H_2}$			
NaMg (Pnma)	−723.6797	−722.2338	−3.6845	−4.2028
$Li_{0.25}Na_{0.75}Mg$ *(Pnma)*	−646.4214	−645.1281	−3.2178	−3.6341
$Li_{0.5}Na_{0.5}Mg$ *(Pnma)*	−569.1746	−568.0249	−2.6259	−3.0559
$Li_{0.625}Na_{0.375}Mg$ *(R3c)*	−530.5490	−529.4696	−2.37288	−2.8273
$Li_{0.75}Na_{0.25}Mg$ *(R3c)*	−491.9194	−490.9116	−2.1796	−2.6436
LiMg (R3c)	−414.6563	−413.7916	−1.9483	−2.4436

$$E_{Bind} = E_{Na_{1-x}Li_xMgH_3} - E_{Na_{1-x}Li_xMgH1_{3-\sigma}} - \frac{\sigma}{2}E_{H_2} \quad (11)$$

E_{Bind} is the hydrogen binding energy, $E_{Na1\text{-}xLi_xMgH_3}$ is the total energy of the fully hydrogenated compound, $E_{Na1\text{-}xLi_xMgH3\text{-}\sigma}$ is the total energy of the compound after removing σ hydrogen molecules, $E(H_2)$ is the energy of an isolated hydrogen molecule, and σ represents the number of hydrogen molecules removed, where σ = 1, 2, 3.

The binding energy (E_{Bind}) is crucial for understanding the strength of the hydrogen-metal interaction, which directly influences hydrogen desorption and the material's suitability for hydrogen storage applications. The analysis of the total energy and binding energy from Fig. 4 and Table 5 shows that increasing lithium concentration leads to more negative total energy values, signifying greater material stability.

For x = 0 ($NaMgH_2$), the total energy is −726.1733 Ryd (GGA) and − 724.7358 Ryd (LDA), whereas at x = 1 ($LiMgH_2$), the total energy becomes −417.0313 Ryd (GGA) and − 416.1723 Ryd (LDA), reflecting the increased stability with higher lithium content. In addition, the binding energy decreases with increasing lithium concentration. For $NaMgH_2$, the binding energy at σ = 1 is −0.9143 eV (GGA) and − 1.0463 eV (LDA), while for $LiMgH_2$, it drops to −0.7918 eV (GGA) and − 0.9374 eV (LDA).

This reduction in binding energy suggests that hydrogen desorption is facilitated at higher lithium concentrations, as the hydrogen-metal bond weakens, allowing the material to release hydrogen more easily. As the desorption stages progress from σ = 1 to σ = 3, the binding energy becomes more negative, indicating stronger hydrogen-metal interactions at higher desorption stages. For x = 0, the binding energy at σ = 3 increases to −3.6845 eV (GGA) and − 4.2028 eV (LDA), reflecting stronger hydrogen bonding at higher desorption stages. In contrast, at x = 1, the binding energy decreases significantly to −1.9483 eV (GGA) and − 2.4436 eV (LDA), suggesting weaker hydrogen-metal interactions, which facilitate hydrogen release under moderate pressures—ideal for hydrogen storage applications.

From this analysis, it is evident that the ***Pnma*** phase is energetically favorable at lower lithium concentrations ($x < 0.625$), while the ***R3c*** phase becomes energetically preferable at higher lithium concentrations ($x \geq 0.625$). This transition is reflected in the changes in both total and binding energy, indicating a composition-induced phase transformation that can be leveraged to optimize the thermodynamic and structural properties of $Na_{1-x}Li_xMgH_3$ alloys for hydrogen storage. The ***R3c*** structure, dominant at higher lithium concentrations, facilitates easier hydrogen desorption due to reduced binding energy, which is advantageous for hydrogen storage systems that require low-pressure hydrogen release.

Thus, the composition-induced phase transformation from ***Pnma*** to ***R3c*** enhances the material's performance for hydrogen storage by balancing material stability with efficient hydrogen release. This approach offers a promising pathway for tuning the thermodynamic and structural properties of $Na_{1-x}Li_xMgH_3$ alloys, making them highly efficient for practical hydrogen storage applications.

3.5. Cohesive energy of $Na_{1-x}Li_xMgH_3$ alloys

The cohesive energy or the bonding energy is considered as another important parameter for stability investigations. In order to calculate the cohesive energy of $Na_{1-x}Li_xMgH_3$ (x = 0, 0.25, 0.5, 0.625, 0.75, 1) alloys we can use the following formula [7,71].

$$E_{coh} = E_{total}^{Na_{1-x}Li_xMgH_3} - \left(xE_{atom}^{Li} + (1-x)E_{atom}^{Na} + E_{atom}^{Mg} + 3E_{atom}^{H}\right) \quad (12)$$

In this equation, $E_{total}^{Na_{1-x}Li_xMgH_3}$ represents the equilibrium total energy of the $Na_{1-x}Li_xMgH_3$ (x = 0, 0.25, 0.5, 0.625, 0.75, 1) alloys in its most stable structural phase, and E_{atom}^{Li}, E_{atom}^{Na}, E_{atom}^{Mg}, and E_{atom}^{H} denote the total

Table 6
The cohesive energy (eV) of $Na_{1-x}Li_xMgH_3$ ($x = 0, 0.25, 0.5, 0.625, 0.75, 1$) as a function of lithium composition, in the most stable phase for GGA and LDA.

Alloys	Cohesive energy (eV)	
	GGA	LDA
$NaMgH_3$(Pnma)	−13.77	−14.36
$Li_{0.25}Na_{0.75}MgH_3$ (Pnma)	−13.93	−14.53
$Li_{0.5}Na_{0.5}MgH_3$ (Pnma)	−14.12	−14.73
$Li_{0.625}Na_{0.375}MgH_3$ (R3c)	−14.23	−14.838
$Li_{0.75}Na_{0.25}MgH_3$ (R3c)	−14.36	−14.95
$LiMgH_3$ (R3c)	−14.67	−15.29

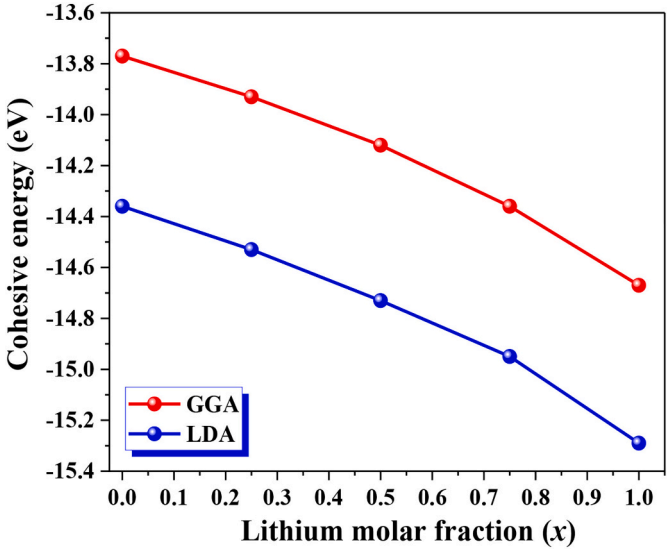

Fig. 5. The cohesive energy (eV) of $Na_{1-x}Li_xMgH_3$ ($x = 0, 0.25, 0.5, 0.625, 0.75, 1$) as a function of lithium composition, calculated using GGA and LDA approximations.

energies of the isolated Li, Na, Mg, and H atoms, respectively.

The cohesive energies of $Na_{1-x}Li_xMgH_3$ ($x = 0, 0.25, 0.5, 0.625, 0.75, 1$) alloys, calculated using both GGA and LDA approximations, are presented in Table 6 and illustrated in Fig. 5. The cohesive energy calculations for $Na_{1-x}Li_xMgH_3$ ($x = 0$–1) alloys reveal systematic trends in structural stability. As shown in Table 6 and Fig. 5, cohesive energies increase monotonically with increasing Li content, from −13.77 eV (GGA) for $NaMgH_3$ ($x = 0$) to −14.67 eV for $LiMgH_3$ ($x = 1$), indicating enhanced thermodynamic stability with Li substitution. This trend, consistent across both GGA and LDA approximations (with LDA predictably yielding more negative values), correlates with Li's smaller ionic radius and higher electronegativity, which strengthen metal-hydrogen interactions.

The stability landscape shows composition-dependent structural preferences. Sodium-rich compositions ($x \leq 0.5$) stabilize in ***Pnma*** symmetry, with cohesive energies of −13.93 eV ($x = 0.25$) and − 14.12 eV ($x = 0.5$). Beyond $x = 0.625$, the system transitions to ***R3c*** symmetry, showing further stabilization to −14.23 eV ($x = 0.625$), −14.36 eV ($x = 0.75$), and − 14.67 eV ($x = 1$). This smooth transition, evident in Fig. 5, suggests both symmetries represent genuine energy minima for their respective composition ranges, with no metastable configurations. While our results (−13.77 to −14.67 eV, GGA) differ in magnitude from Xiao et al.'s [7] values (−10.43 to −10.92 eV) due to methodological variations, both studies confirm the stabilizing effect of Li substitution. The consistent energy-composition relationship, particularly the linear stabilization trend across the phase transition, indicates stability is primarily composition-driven. These findings establish a robust framework for designing optimized hydride systems, where stability can be

Table 7
Calculated atomic positions of $Na_{1-x}Li_xMgH_3$ ($x = 0, 0.25, 0.5, 0.625, 0.75, 1$) alloys using the GGA and LDA approximations.

Atomic positions		
Alloys	*GGA*	*LDA*
$NaMgH_3$ (Pnma)	Na (0.5304, 0.25, 0.0055), Mg (0.5, 0.0, 0,5) H 1 (0.7932, 0.0435, 0.2948), H 2 (0.9726, 0.25,0.9166) Li 1 (0.9825, 0.2523, 0.25), Li 2 (0.2321, 0.4970, 0.25)	Na (0.5304, 0.25, 0.0055), Mg (0.5, 0.0, 0,5) H 1 (0.7932, 0.0435, 0.2948), H 2 (0.9726, 0.25,0.9166) Li 1 (0.9814, 0.2517, 0.25), LI 2 (0.2308, 0.4974, 0.25)
$Li_{0.25}Na_{0.75}MgH_3$ (Pnma)	Na 1 (0.4833, 0.2529, 0.25), Na 2 (0.7358, 0.4987, 0.25) Na 3 (0.9850, 0.7531, 0.25), Na 4 (0.2349, 0.9962, 0.25) Na 5 (0.4857, 0.7513, 0.25), Na 6 (0.7351, 0.9984, 0.25) Mg 1 (0.0, 0.5, 0.0), Mg 2 (0.2465, 0.2498, 0.4951) Mg 3 (0.7517, 0.2541, 0.5000), Mg 4 (0.0, 0.0, 0.0) Mg 5 (0.5, 0.0, 0.0), Mg 6 (0.5, 0.5, 0.0) H 1 (0.8533, 0.4006, 0.0452), H 2 (0.9035, 0.6530, 0.5533) H 3 (0.3457, 0.4024, 0.0531), H 4 (0.3989, 0.6477, 0.5454) H 5 (0.8531, 0.8996, 0.0461), H 6 (0.8964, 0.1478, 0.5467) H 7 (0.3527, 0.8944, 0.0439), H 8 (0.3960, 0.1486, 0.5429) H 9 (0.7655, 0.7075, 0.25), H 10 (0.0165, 0.5442, 0.25) H 11 (0.2623, 0.6960, 0.25), H 12 (0.5177, 0.5432, 0.25) H 13 (0.7679, 0.2107, 0.25), H 14 (0.0119, 0.0525, 0.25) H 15 (0.2640, 0.2046, 0.25), H 16 (0.5135, 0.0408, 0.25) Li 1 (0.9799, 0.2510, 0.25), Li 2 (0.2330, 0.5003, 0.25) Li 3 (0.4799, 0.2510, 0.25), Li 4 (0.7330, 0.5003, 0.25)	Na 1 (0.4807, 0.2527, 0.25), Na 2 (0.7339, 0.4984, 0.25) Na 3 (0.9842, 0.7531, 0.25), Na 4 (0.2331, 0.9953, 0.25) Na 5 (0.4844, 0.7526, 0.25), Na 6 (0.7345, 0.9990, 0.25) Mg 1 (0.0, 0.5, 0.0), Mg 2 (0.2446, 0.2506, 0.4944) Mg 3 (0.7519, 0.2552, 0.5005), Mg 4 (0.0, 0.0, 0.0) Mg 5 (0.5, 0.0, 0.0), Mg 6 (0.5, 0.5, 0.0) H 1 (0.8520, 0.4028, 0.0468), H 2 (0.9079, 0.6565, 0.5584) H 3 (0.3419, 0.4054, 0.0587, H 4 (0.4006, 0.6486, 0.5472) H 5 (0.8525, 0.9009, 0.0481), H 6 (0.8963, 0.1481, 0.5500) H 7 (0.3525, 0.8934, 0.0448), H 8 (0.3958, 0.1494, 0.5429) H 9 (0.7672, 0.7064, 0.25), H 10 (0.0191, 0.5460, 0.25) H 11 (0.2624, 0.6891, 0.25), H 12 (0.5209, 0.5450, 0.25) H 13 (0.7715, 0.2111, 0.25), H 14 (0.0119, 0.0588, 0.25) H 15 (0.2650, 0.2020, 0.25), H 16 (0.5142, 0.0410, 0.25) Li 1 (0.9798, 0.2509, 0.25), Li 2 (0.2330, 0.5006, 0.25) Li 3 (0.4798, 0.2509, 0.25), Li 4 (0.7330, 0.5006, 0.25)
$Li_{0.5}Na_{0.5}MgH_3$ (Pnma)	Na1 (0.9861, 0.7530, 0.25), Na 2 (0.2355, 0.9984, 0.25) Na 3 (0.4861, 0.7530, 0.25), Na 4 (0.7355, 0.9984, 0.25) Mg 1 (0.0, 0.5, 0.0), Mg 2 (0.2470, 0.2567, 0.4943) Mg 3 (0.7470, 0.2567, 0.4943), Mg 4 (0.0, 0.0, 0.0) Mg 5 (0.5, 0.0, 0.0), Mg 6 (0.5, 0.5, 0.0) H 1 (0.8413, 0.4117, 0.0617), H 2 (0.9115, 0.6576, 0.5613) H 3 (0.3413, 0.4117, 0.0617), H 4 (0.4115,	Na 1 (0.9849, 0.7535, 0.25), Na 2 (0.2343, 0.9978, 0.25) Na 3 (0.4849, 0.7535, 0.25), Na 4 (0.7343, 0.9978, 0.25) Mg 1 (0.0, 0.5, 0.0), Mg 2 (0.2471, 0.2563, 0.4946) Mg 3 (0.7471, 0.2563, 0.4946), Mg 4 (0.0, 0.0, 0.0) Mg 5 (0.5, 0.0, 0.0), Mg 6 (0.5, 0.5, 0.0) H 1 (0.8413, 0.4114, 0.0615), H 2 (0.9114, 0.6577, 0.5608) H 3 (0.3413, 0.4114, 0.0615), H 4 (0.4114,

(*continued on next page*)

Table 7 (*continued*)

Atomic positions		
Alloys	*GGA*	*LDA*
	0.6576, 0.5613) H 5 (0.8527, 0.8960, 0.0484), H 6 (0.8945, 0.1499, 0.5482) H 7 (0.3527, 0.8960, 0.0484), H 8 (0.3945, 0.1499, 0.5482) H 9 (0.7663, 0.6870, 0.25), H 10 (0286, 0.5480, 0.25) H 11 (0.2663, 0.6870, 0.25), H 12 (0.5286, 0.5480, 0.25) H 13 (0.7743, 0.2066, 0.25), H 14 (0.0120, 0.0577, 0.25) H 15 (0.2743, 0.2066, 0.25), H 16 (0.5120, 0.0577, 025)	0.6577, 0.5608) H 5 (0.8524, 0.8964, 0.0489), H 6 (0.8948, 0.1497, 0.5490) H 7 (0.3524, 0.8964, 0.0489), H 8 (0.3948, 0.1497, 0.5490) H 9 (0.7669, 0.6874, 0.25), H 10 (0.0288, 0.5484, 0.25) H 11 (0.2669, 0.6874, 0.25), H 12 (0.5288, 0.5484, 0.25) H 13 (0.7745, 0.2059, 0.25), H 14 (0.0126, 0.0577, 0.25) H 15 (0.2745, 0.2059, 0.25), H 16 (0.5126, 0.0577, 0.25)
$Li_{0.625}Na_{0.375}MgH_3$ *(R3c)*	Na 1 (0.9340, 0.7403, 0.7410), Na 2 (0.4348, 0.7368, 0.7380) Na 3 (0.6848, 0.7406, 0.7414) Li 1 (0.1791, 0.7071, 0.71174), Li 2 (0.8018, 0.2027, 0.2032) Li 3 (0.3001, 0.2042, 0.2153), Li 4 (0.5488, 0.2083, 0.2072) Li 5 (0.0545, 0.2065, 0.1950) Mg 1 (0.8790, 0.5025, 0.5054), Mg 2 (0.3692, 0.5214, 0.5137) Mg 3 (0.6264, 0.5086, 0.5082) Mg 4 (0.1306, 0.4915, 0.4939) Mg 5 (0.7492, 0.9979, 0.9986), Mg 6 (0.2450, 0.0043, 0.0107) Mg 7 (0.4973, 0.9993, 0.0006), Mg 8 (0.0065, 0.9907, 0.9835) H 1 (0.9057, 0.2665, 0.9014), H 2 (0.3993, 0.2802, 0.9018) H 3 (0.6516, 0.2771, 0.9046), H 4 (0.1484, 0.3165, 0.9084) H 5 (0.7924, 0.3432, 0.7924), H 6 (0.2732, 0.3996, 0.8136) H 7 (0.5410, 0.3429, 0.7954), H 8 (0.0406, 0.3584, 0.7924) H 9 (0.8199, 0.9010, 0.6078), H 10 (0.3188, 0.9131, 0.6159) H 11 (0.5690, 0.9052, 0.6083), H 12 (0.0773, 0.9010, 0.5868) H 13 (0.9541, 0.1542, 0.3399), H 14 (0.4447, 0.1749, 0.3475) H 15 (0.6988, 0.1656, 0.3442), H 16 (0.1996, 0.0955, 0.4124) H 17 (0.9778, 0.6093, 0.2729), H 18 (0.4730, 0.6092, 0.2816) H 19 (0.7262, 0.6060, 0.2776), H 20 (0.2277, 0.5944, 0.3092)	Na 1 (0.9339, 0.7390, 0.7402), Na 2 (0.4345, 0.7359, 0.7375) Na 3 (0.6846, 0.7400, 0.7404) Li 1 (0.1789, 0.7066, 0.7114), Li 2 (0.8013, 0.2013, 0.2016) Li 3 (0.2994, 0.2034, 0.2151), Li 4 (0.5486, 0.2068, 0.2055), Li 5 (0.0546, 0.2051, 0.1934) Mg 1 (0.8795, 0.5039, 0.5074), Mg 2 (0.3696, 0.5226, 0.5158) Mg 3 (0.6268, 0.5104, 0.5101) Mg 4 (0.1307, 0.4926, 0.4939) Mg 5 (0.7490, 0.9973, 0.9980), Mg 6 (0.2451, 0.0041, 0.0105) Mg 7 (0.4972, 0.9987, 0.9998), Mg 8 (0.0064, 0.9905, 0.9836) H 1 (0.9069, 0.2662, 0.8983), H 2 (0.3999, 0.2808, 0.8990) H 3 (0.6525, 0.2777, 0.9012), H 4 (0.1487, 0.3160, 0.9077) H 5 (0.7915, 0.3450, 0.7912), H 6 (0.2734, 0.3984, 0.8118) H 7 (0.5402, 0.3447, 0.7940), H 8 (0.0402, 0.3605, 0.7912) H 9 (0.8200, 0.8983, 0.6109), H 10 (0.3184, 0.9103, 0.6214) H 11 (0.5692, 0.9020, 0.6114), H 12 (0.0774, 0.8997, 0.5874) H 13 (0.9539, 0.1507, 0.3410), H 14 (0.4443, 0.1725, 0.3492) H 15 (0.6985, 0.1624, 0.3457), H 16 (0.1991, 0.0972, 0.4118) H 17 (0.9770, 0.6130, 0.2730), H 18 (0.4723, 0.6122, 0.2821) H 19 (0.7254, 0.6095, 0.2780), H 20 (0.2275, 0.5967, 0.3075)

Table 7 (*continued*)

Atomic positions		
Alloys	*GGA*	*LDA*
	H 21 (0.8363, 0.7908, 0.1677), H 22 (0.3367, 0.8186, 0.1482) H 23 (0.5852, 0.7960, 0.1663), H 24 (0.1026, 0.7881, 0.1071)	H 21 (0.8367, 0.7898, 0.1642), H 22 (0.3369, 0.8188, 0.1444) H 23 (0.5858, 0.7947, 0.1629), H 24 (0.1024, 0.7846, 0.1103)
$Li_{0.75}Na_{0.25}MgH_3$ *(R3c)*	Li 1 (0.1063, 0.2095, 0.2003), Li 2 (0.6012, 0.2057, 0.2136) Li 3 (0.3568, 0.7091, 0.7125) Na 1 (0.8657, 0.7310 0.7350) Mg 1 (0.0074, 0.9920, 0.9896), Mg 2 (0.4910, 0.0035, 0.0087) Mg 3 (0.2596, 0.4938, 0.4940), Mg 4 (0.7434, 0.513, 0.5135) H 1 (0.2038, 0.7902, 0.1098), H 2 (0.6759, 0.8193, 0.1420) H 3 (0.4546, 0.5969, 0.3079), H 4 (0.9504, 0.6101, 0.2794) H 5 (0.3998, 0.0976, 0.4098), H 6 (0.9034, 0.1538, 0.3493) H 7 (0.1541, 0.9016, 0.5902), H 8 (0.6389, 0.9087, 0.6162) H 9 (0.0768, 0.3612, 0.7996), H 10 (0.5484, 0.3982, 0.8100) H 11 (0.2980, 0.3137, 0.9073), H 12 (0.8054, 0.2732, 0.9007)	Li 1 (0.1057, 0.2093, 0.1997), Li 2 (0.6010, 0.2045, 0.2131) Li 3 (0.3565, 0.7083, 0.7119) Na 1 (0.8648, 0.7295, 0.7332) Mg 1 (0.0075, 0.9924, 0.9901), Mg 2 (0.4914, 0.0040, 0.0091) Mg 3 (0.2593, 0.4945, 0.4951), Mg 4 (0.7440, 0.5136, 0.5130) H 1 (0.2032, 0.7896, 0.1111), H 2 (0.6766, 0.8182, 0.1420) H 3 (0.4539, 0.5988, 0.3067), H 4 (0.9502, 0.6111, 0.2784) H 5 (0.3993, 0.0995, 0.4088), H 6 (0.9031, 0.1534, 0.3505) H 7 (0.1536, 0.9008, 0.5922), H 8 (0.6384, 0.9077, 0.6170) H 9 (0.0766, 0.3622, 0.7994), H 10 (0.5494, 0.3975, 0.8083) H 11 (0.2989, 0.3122, 0.9063), H 12 (0.8059, 0.2728, 0.8999)
$LiMgH_3$ *(R3c)*	Li 1 (0.2108, 0.2108, 0.2108), Li 2 (0.7108, 0.7108, 0.7108) Mg 1 (0.0, 0.0, 0.0), Mg 2 (0.5000, 0.5000, 0.5000) H 1 (0.4021, 0.8022, 0.1048), H 2 (0.9021, 0.6048, 0.3022) H 3 (0.8022, 0.1048, 0.4021), H 4 (0.3022, 0.9021, 0.6048) H 5 (0.1048, 0.4021, 0.8022), H 6 (0.6048, 0.3022, 0.902)	Li 1 (0.2108, 0.2108, 0.2108), Li 2 (0.7108, 0.7108, 0.7108) Mg 1 (0.0, 0.0, 0.0), Mg 2 (0.5000, 0.5000, 0.5000) H 1 (0.4021, 0.8022, 0.1048), H 2 (0.9021, 0.6048, 0.3022) H 3 (0.8022, 0.1048, 0.4021), H 4 (0.3022, 0.9021, 0.6048) H 5 (0.1048, 0.4021, 0.8022), H 6 (0.6048, 0.3022, 0.9021)

precisely tuned through Li/Na ratio control, with important implications for hydrogen storage applications that require careful balance between thermodynamic stability and kinetic properties.

3.6. Total energy calculations and phase transition of $Na_{1-x}Li_xMgH_3$

The structural stability and bonding characteristics of each alloy configuration were investigated through full atomic relaxation. Structural optimizations were carried out using both LDA and GGA exchange-correlation approximations to ensure robustness of the results. The final optimized atomic positions for each composition and structural phase are listed in Table 7. Fig. 6 illustrates the structural evolution of $Na_{1-x}Li_xMgH_3$ (x = 0, 0.25, 0.5, 0.625, 0.75, 1), revealing a clear phase transition from the orthorhombic ***Pnma*** phase to the rhombohedral ***R3c*** phase as the Li concentration increases. This transformation is accompanied by notable structural distortions, variations in octahedral tilting, and significant changes in the hydrogen coordination environment factors that directly affect the material's hydrogen storage performance.

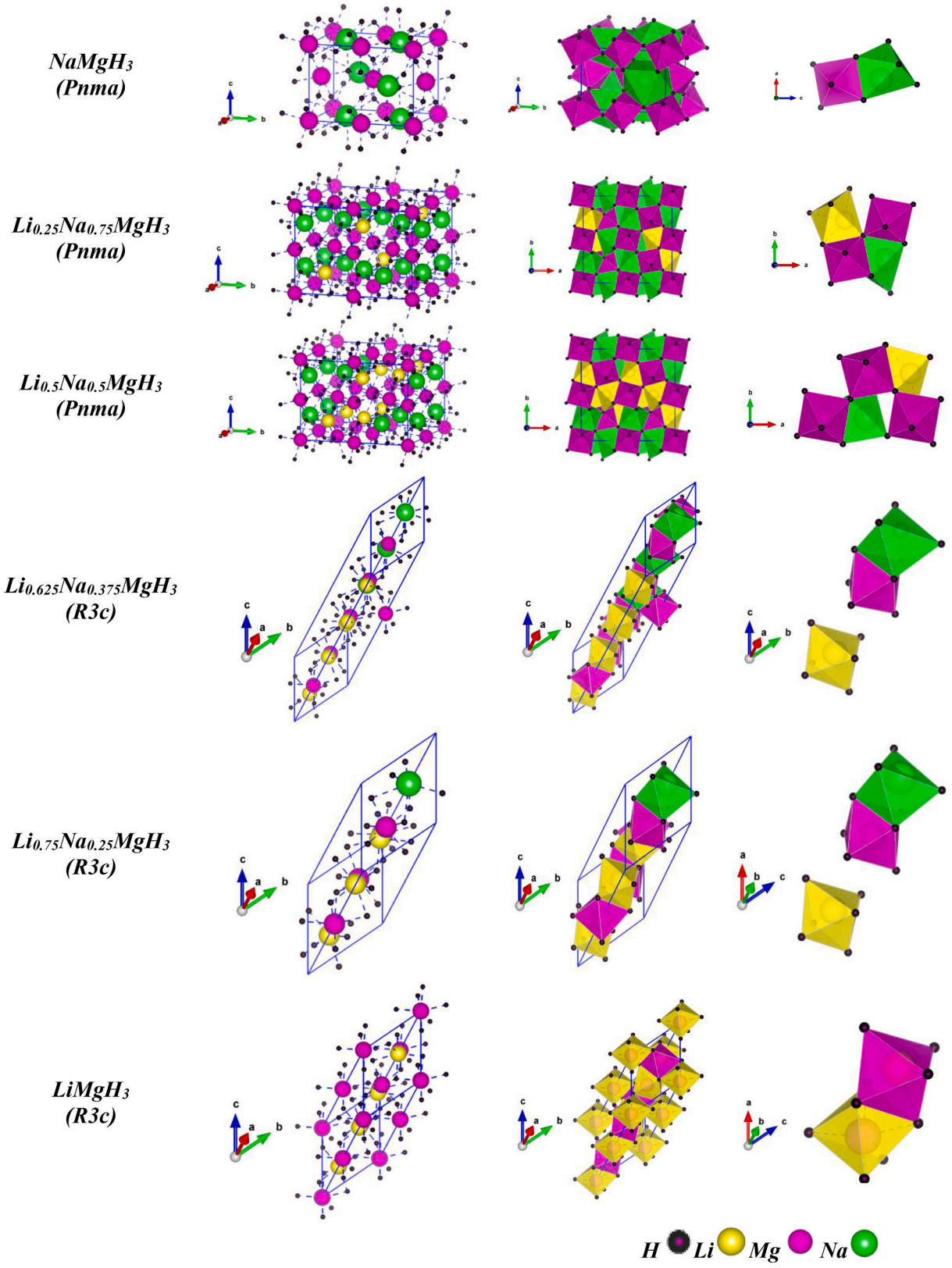

Fig. 6. The different structural phases of $Na_{1-x}Li_xMgH_3$ ($x = 0$, 0.25, 0.5, 0.625, 0.75, 0.875, 1).

For $NaMgH_3$ ($x = 0$), the structure adopts a perovskite-like orthorhombic ***Pnma*** phase. In this configuration, Na^+ cations are octahedrally coordinated by H^-anions in a distorted environment. Mg^{2+}cations form corner-sharing MgH_6 octahedra, exhibiting tilt angles between 27° and 30°. Hydrogen atoms occupy two inequivalent Wyckoff positions, contributing to an anisotropic and complex hydrogen bonding network. As Li is incrementally substituted into the lattice at $x = 0.25$ and $x = 0.5$, the structure retains the ***Pnma*** symmetry. The mixed Na/Li occupancy introduces mild distortions in the local coordination geometry, while the MgH_6 octahedra maintain their corner-sharing connectivity.

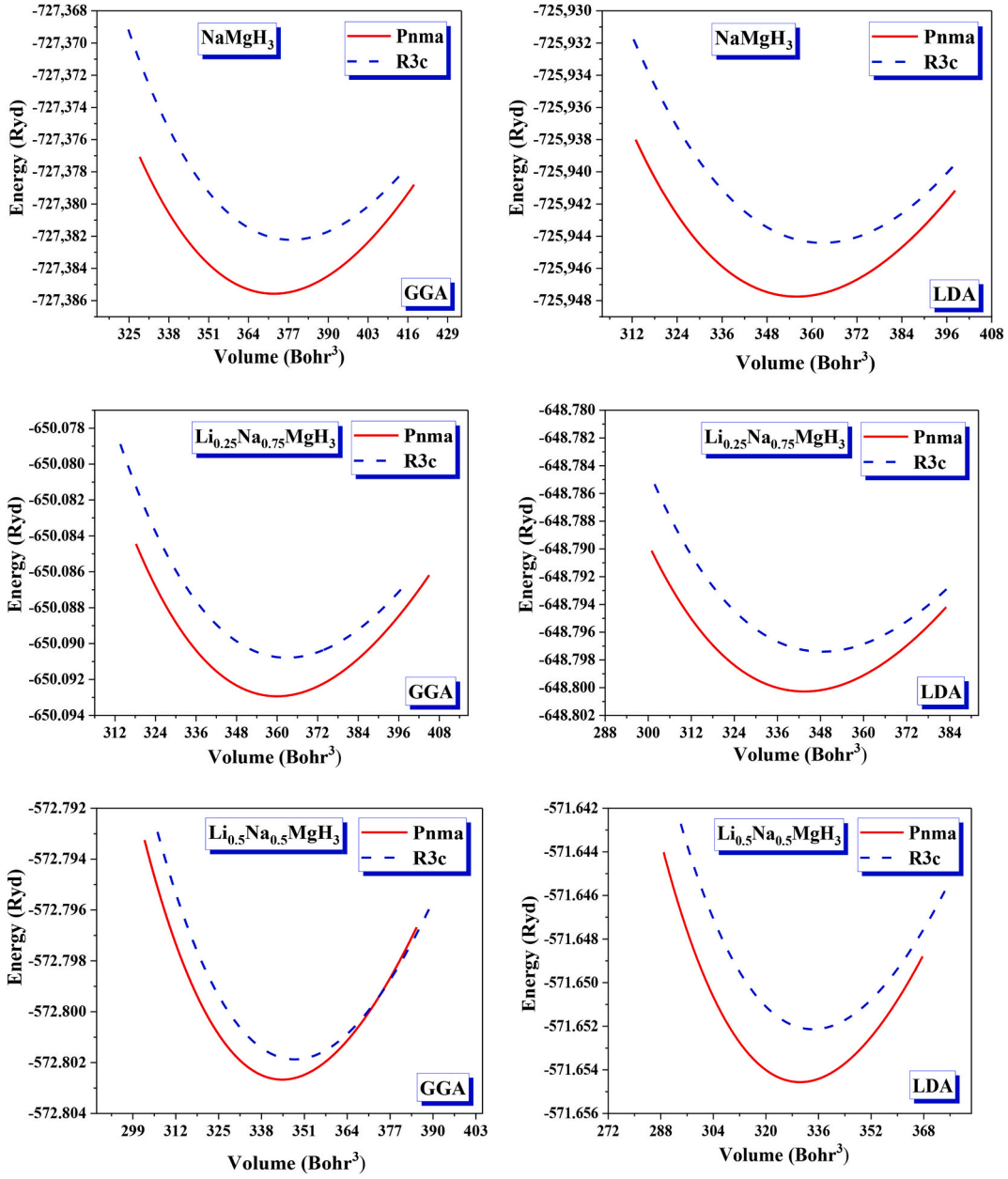

Fig. 7. Variation of the total energy as a function of unit cell volume for the $Na_{1-x}Li_xMgH_3$ alloys at $x = 0$, 0.25, 0.5, 0.625, 0.75, 1, in the ***Pnma*** and ***R3c*** phases, using GGA and LDA approximations.

Bond lengths and tilt angles remain relatively stable, indicating a gradual accommodation of Li into the lattice without immediate structural disruption. At $x = 0.625$, a structural phase transition emerges, shifting the symmetry from ***Pnma*** to ***R3c***. This transition is marked by increased octahedral tilting, altered polyhedral connectivity, and enhanced distortion in both the (Na/Li)-H and H-Mg-H bonding frameworks. The increased Li content leads to a reduction in lattice parameters and modifies the hydrogen bonding environment. These changes are particularly important as they influence the electronic structure and phonon dynamics, thereby impacting hydrogen diffusion pathways and desorption kinetics.

For higher Li concentrations ($x = 0.75$ and $x = 1$), the structure stabilizes in the rhombohedral ***R3c*** phase. In these compositions, the LiH_6 and MgH_6 octahedra exhibit stronger tilting and enhanced interaction. A notable structural trend is the progressive **s**hortening of the (Na/Li)–H bond lengths with increasing Li content, reflecting stronger Li—H interactions and a denser hydrogen network. At $x = 1$ ($LiMgH_3$), the compound crystallizes fully in the ***R3c*** trigonal phase. Li^+ ions form distorted Li H_6 octahedra that share corners, edges, and faces with adjacent MgH_6 octahedra. This high degree of octahedral connectivity promotes a compact and interconnected hydrogen framework, which is anticipated to enhance both the hydrogen storage capacity and kinetic performance. The structural contraction and increased bonding strength with rising Li content make the $Na_{1-x}Li_xMgH_3$ series a promising candidate for reversible hydrogen storage applications.

To determine the structural properties of $Na_{1-x}Li_xMgH_3$ ($x = 0$, 0.25, 0.5, 0.625, 0.75, 1) at static equilibrium, we calculated the total energy E for various unit cell volumes. These energy volume data were then fitted using the Murnaghan equation of state (EOS) [46] to extract equilibrium lattice parameters, bulk modulus B, its pressure derivative B', unit cell volume V, and minimum energy E_0, using both LDA and GGA approximations.

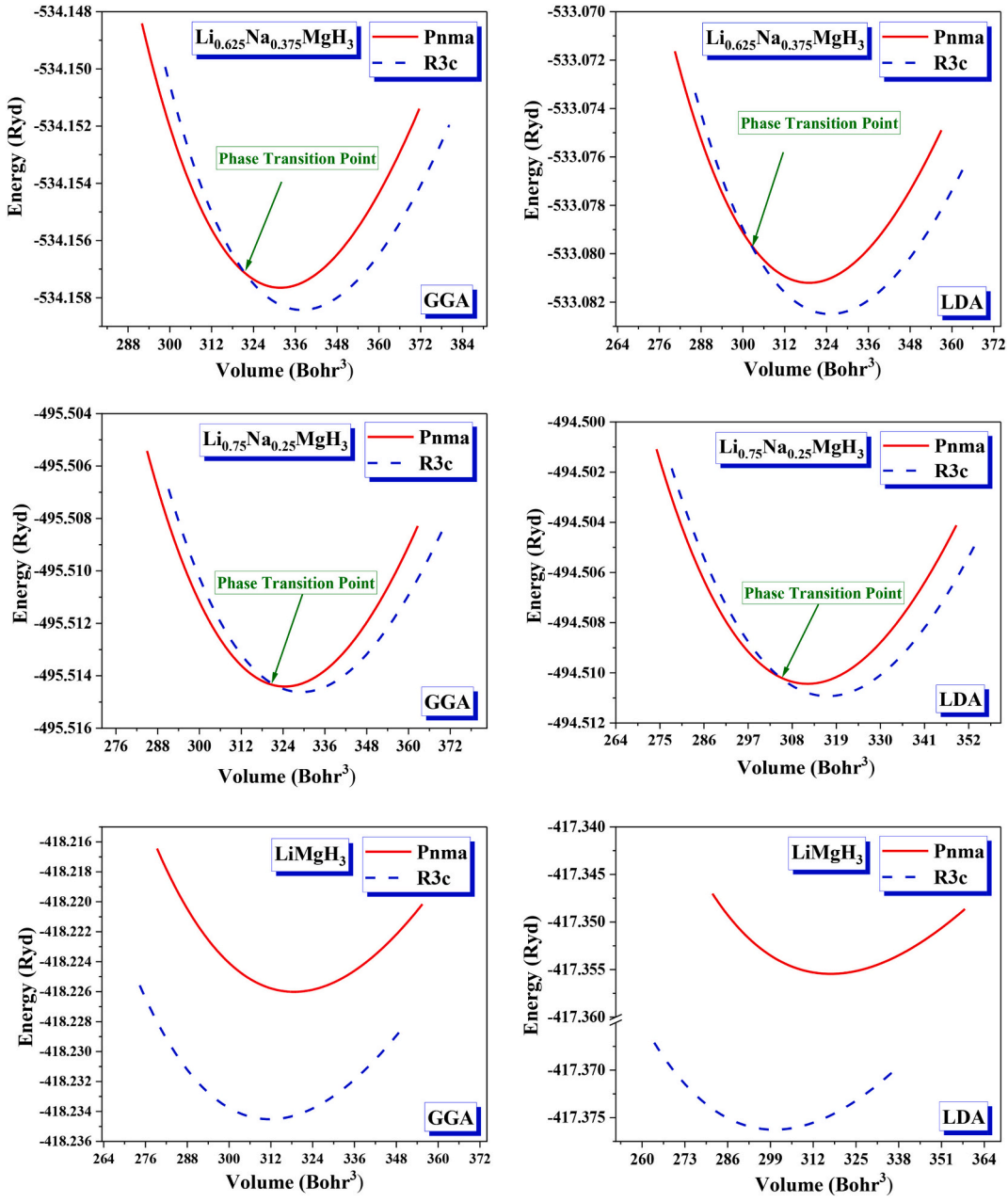

Fig. 7. (*continued*).

Fig. 7 presents the EOS curves and highlights the phase transition behavior. For compositions with $x = 0$, 0.25, and 0.5, the orthorhombic ***Pnma*** phase is more stable than the ***R3c*** phase, as evidenced by its lower total energy. However, for $x = 0.625$, a crossover between the ***Pnma*** and ***R3c*** energy curves is observed, indicating a structural phase transition. This trend continues for $x = 0.75$ and $x = 1$, where the rhombohedral ***R3c*** phase becomes energetically favored, suggesting it is the most stable phase at high Li content. The optimized structural parameters for all compositions are summarized in Table 8.

Our primary focus was on identifying the most stable crystalline phases and assessing their lattice constants (a, b, c), volumes, bulk moduli (B), pressure derivatives (B'), and ground-state energies. The reliability of our results was confirmed through a comparison of the calculated lattice parameters with experimental data, yielding relative errors within acceptable bounds. For $NaMgH_3$ ($x = 0$), the computed volume of 221.23 $Å^3$ is in reasonable agreement with the experimental value of 230.49 $Å^3$ reported by Vasquez et al. [38], showing a relative error of approximately 4 %.

The GGA approximation yields lattice parameters $a = 5.4228$ Å, $b = 7.6002$ Å, and $c = 5.3678$ Å. These values are close to the experimental data of Ikeda [22] ($a = 5.463$ Å, $b = 7.701$ Å, $c = 5.409$ Å) and Martinez-Coronadoa [39] ($a = 5.465$ Å, $b = 7.626$ Å, $c = 5.413$ Å), with small deviations of about 0.7–0.8 %. This demonstrates the accuracy of the GGA approximation in capturing the structural features of $NaMgH_3$. For $Li_{0.5}Na_{0.5}MgH_3$($x = 0.5$), the GGA approximation produced lattice parameters $a = 5.2891$ Å, $b = 7.4452$ Å, and $c = 5.1750$ Å, which are in good agreement with the experimental values from Ikeda [22] ($a = 5.460$ Å, $b = 7.698$ Å, $c = 5.399$ Å) and Contreras Vasquez [38] ($a = 5.45$ Å, $b = 7.675$ Å, $c = 5.393$ Å). The relative deviations in the lattice constants are minimal, typically under 3 %, indicating that the GGA approximation provides a reliable description for $Li_{0.5}Na_{0.5}MgH_3$. For $LiMgH_3$ ($x = 1$), crystallizing in the rhombohedral ***R3c*** structure, the GGA approximation yielded lattice parameters $a = 5.2505$ Å and $\alpha = 55.80°$. These are in reasonable agreement with the computed values of

Table 8
Calculated values of the lattice constants (a, b, c), bulk modulus (B), bulk modulus derivative (B'), equilibrium volume (V), and minimum total energy (E_0) using the GGA and LDA approximations for $Na_{1-x}Li_xMgH_3$ ($x = 0$, 0.25, 0.5, 0.625, 0.75, 1) alloys in their most stable phases.

Alloys	*GGA*			*LDA*
$NaMgH_3$ *(Pnma)*	a (Å)		5.4228, 5.463[a], 5.452[b], 5.465[c], 5.484[d], 5.409[e], 5.430[f] [I] 5.487, [J]5,463	5.3463
	Relative Error in a		$\left.\frac{\Delta a}{a}\right\|_{exp(a)} = 0.73\%$, $\left.\frac{\Delta a}{a}\right\|_{exp(c)} = 0.78\%$	$\left.\frac{\Delta a}{a}\right\|_{exp(a)} = 2.14\%$, $\left.\frac{\Delta a}{a}\right\|_{exp(c)} = 2.17\%$
	b (Å)		7.6002, 7.703[a], 7.695[b], 7.737[d], 7.626[e],7.629[f], 7.661[I], 7.701 [J]	7.5056
	Relative Error in b		$\left.\frac{\Delta b}{b}\right\|_{exp(a)} = 1.33\%$, $\left.\frac{\Delta b}{b}\right\|_{exp(c)} = 1.29\%$	$\left.\frac{\Delta b}{b}\right\|_{exp(a)} = 2.55\%$, $\left.\frac{\Delta b}{b}\right\|_{exp(c)} = 2.55\%$
	c (Å)		5.3678, 5.410[a] 5.368[b] 5.413[c] 5.425[d], 5.332[e] 5.340[f], 5.395[I], 0.5409 [J]	5.2524
	Relative Error in c		$\left.\frac{\Delta c}{c}\right\|_{exp(a)} = 0.77\%$, $\left.\frac{\Delta c}{c}\right\|_{exp(c)} = 0.84\%$	$\left.\frac{\Delta c}{c}\right\|_{exp(a)} = 2.92\%$, $\left.\frac{\Delta c}{c}\right\|_{exp(c)} = 2.97\%$
	b/a		1.4015	1.4038
	c/a		0.9898	0.9824
	$V(Å^3)$		221.2304,227.88[c], [I]226.78	210.7640
	B(GPa)		41.6549, 37.47[f], 38.4[b] 39.78[I]	45.4392
	B'		3.5922, [I]3.60	3.7729
	E_0 (Ryd)		−727.3850, [I]-729.1074	−725.9476
$Li_{0.25}Na_{0.75}MgH_3$ *(Pnma)*	a (Å)		5.3674, 5.465[c], *5.408*[f]	5.2793
	Relative Error in a		$\left.\frac{\Delta a}{a}\right\|_{exp(c)} = 1.79\%$	$\left.\frac{\Delta a}{a}\right\|_{exp(c)} = 3.40\%$
	b (Å)		7.5697, 7.702[c], *7.589*[f]	7.4102
	Relative Error in b		$\left.\frac{\Delta b}{b}\right\|_{exp(c)} = 1.72\%$	$\left.\frac{\Delta b}{b}\right\|_{exp(c)} = 3.79\%$
	c (Å)		5.2753, 5.406[c], *5.295*[f]	5.2768
	Relative Error in c		$\left.\frac{\Delta c}{c}\right\|_{exp(c)} = 2.42\%$	$\left.\frac{\Delta c}{c}\right\|_{exp(c)} = 3.40\%$
	b/a		1.4103	1.4036
	c/a		0.9828	0.9995
	$V(Å^3)$		214.3333 227.61[c]	206.4319
	B(GPa)		43.0968, 37.69[f]	46.9237
	B'		3.8873	4.6108
	E_0 (Ryd)		−650.0929	−648.8002
$Li_{0.5}Na_{0.5}MgH_3$ *(Pnma)*	a (Å)		5.2891, 5.364[f], 5.460[c], 5.451[d]	5.2110
	Relative Error in a		$\left.\frac{\Delta a}{a}\right\|_{exp(c)} = 3.13\%$	$\left.\frac{\Delta a}{a}\right\|_{exp(c)} = 3.57\%$
	b (Å)		7.4452, 7.523[f], 7.698[c], 7.675[d]	7.3224
	Relative Error in b		$\left.\frac{\Delta b}{b}\right\|_{exp(c)} = 3.28\%$	$\left.\frac{\Delta b}{b}\right\|_{exp(c)} = 4.88\%$
	c (Å)		5.1750, 5.218[f], 5.399[c], 5.393[d]	5.0992
	Relative Error in c		$\left.\frac{\Delta c}{c}\right\|_{exp(c)} = 4.14\%$	$\left.\frac{\Delta c}{c}\right\|_{exp(c)} = 5.55\%$
	b/a		1.4076	1.4051
	c/a		0.9784	0.9785
	$V(Å^3)$		203.7832 226.96[c]	194.5703
	B(GPa)		44.3373, 38.23[f]	47.6006
	B'		3.7465	3.9570
	E_0 (Ryd)		−572.8026	−571.6545
$Li_{0.625}Na_{0.375}MgH_3$ *(R3c)*	*Hexagonal (conventional unit cell)*	a (Å)	5.0474	4.9825
		c (Å)	13.6149	13.4398
		c/a	2.6974	2.6974
		$V(Å^3)$	300.3865	288.95
	Rhombohedral (primitive unit cell)	a (Å)	5.3934	5.3240
		A	55.80°	55.80°
		$V(Å^3)$	100.1322	96.32
	B(GPa)		43.9405	47.1273
	B'		4.2888	3.9897
	E_0 (Ryd)		−534.1584	−533.0824
$Li_{0.75}Na_{0.25}MgH_3$ *(R3c)*	*Hexagonal (conventional unit cell)*	a (Å)	5.0200, 5.128[f]	4.9564
		c (Å)	13.380, 13.483[f]	13.2432
		c/a	2.6653	2.6719
		$V(Å^3)$	292.0076	93.915
	Rhombohedral (primitive unit cell)	a (Å)	5.3471	5.2791
		A	55,80	55,80
		$V(Å^3)$	97.5754	93.8999
	B(GPa)		43.5332, 38.99[f]	47.9908
	B'		4.2457	4.7521
	E_0 (Ryd)		−495.5145	−494.5117
$LiMgH_3$ *(R3c)*	*Hexagonal (conventional unit cell)*	a (Å)	4.9330, 4.916[f], 4.958[b]	4.8716
		c (Å)	13.2437, 13.257[f],13.337[b]	12.7311
		c/a	2.6847	2.6133
		$V(Å^3)$	279.1014	87.2204
	Rhombohedral (primitive unit cell)	a (Å)	5.2505, 5.311[G], 5.281[H]	5.1849

(*continued on next page*)

Table 8 (*continued*)

Alloys	*GGA*			*LDA*
		A	55.80°, 55.9[G], 55.9[H]	55.80°
		V(Å³)	92.3820, 96.0[G], 94.4[H]	88.9624
	B(GPa)		46.9025, 40.04[f], 39.8[b]	52.5690
	B′		2.5114, 3.1[b]	2.1840
	E_0 (Ryd)		−418.2346	−417.3753

[a] Experimental data of Ref [72].
[b] PP-GGA [33].
[c] Experimental data of Ref [39].
[d] Experimental data of Ref [38].
[e] PP-GGA [7].
[f] PP-GGA [59].
[G] PP-GGA [68].
[H] PP-GGA [73].
[I] PP-GGA [8].
[J] Experimental data of Ref [22]

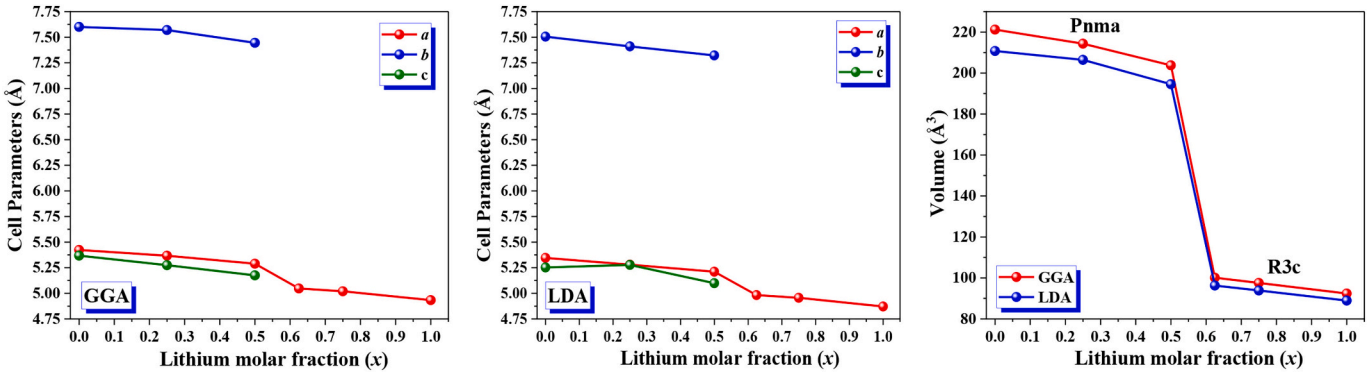

Fig. 8. Calculated lattice constants and volume as a function of lithium concentration for the ***Pnma*** and ***R3c*** phases of $Na_{1-x}Li_xMgH_3$ ($x = 0, 0.25, 0.5, 0.625, 0.75, 1$) using GGA and LDA approximations.

Vajeeston et al. [33] ($a = 5.283$ Å, $\alpha = 55.87°$), with only a small deviation of about 0.6 % in the lattice constant. In addition, the hexagonal representation gave $a = 4.9330$ Å and $c = 13.2437$ Å, which closely match the values obtained by Vajeeston et al. [33] ($a = 4.958$ Å, $c = 13.337$ Å), with relative errors of approximately 0.5 % for a and 0.7 % for c.

This comparison further supports the reliability of the GGA approximation for this composition. We observe a systematic decrease in the equilibrium volume with increasing Li concentration, which is attributed to the smaller ionic radius of Li^+ compared to Na^+. Concurrently, the bulk modulus for the GGA approximation increases from 41.65 GPa ($x = 0$) to 46.90 GPa ($x = 1$), indicating a stiffer, less compressible lattice as Li replaces Na, suggesting enhanced structural rigidity and improved mechanical stability. While both LDA and GGA slightly underestimate lattice parameters, GGA provides a more accurate description, especially in systems with varying ionic sizes. The consideration of electron density gradients in GGA allows it to better capture the effects of Li substitution, aligning with experimental trends in volume and bulk modulus. This improved agreement with experimental data further validates GGA's superiority over LDA in modeling these materials.

Fig. 8 shows the variation in lattice parameters and unit cell volume per formula unit for $Na_{1-x}Li_xMgH_3$ ($x = 0, 0.25, 0.5, 0.625, 0.75, 1$) across the ***Pnma*** and ***R3c*** phases, calculated using both GGA and LDA approximations, as a function of Li substitution. A clear decreasing trend in lattice parameters and cell volume is observed with increasing Li content, which is attributed to the smaller ionic radius of Li^+ compared to Na^+. This contraction as Li substitutes Na in the structure reflects the impact of ionic size on the lattice. The consistent reduction in unit-cell volume across the composition range confirms the reliability of our computational approach. These optimized structural parameters form the foundation for calculating additional physical properties of the compounds.

Table 9 presents the interatomic distances (Å) and bond angles (°) for $Na_{1-x}Li_xMgH_3$ ($x = 0, 0.25, 0.5, 0.625, 0.75, 1$), highlighting the structural effects of Li incorporation. These DFT-based results, obtained using both LDA and GGA approximations, are compared with experimental data from Martínez-Coronado et al. [39] and theoretical findings from Vajeeston et al. [33]. This comparison enables a clear assessment of structural evolution, hydrogen coordination, and bond distortion induced by Li substitution. In $NaMgH_3$ ($x = 0$), the GGA predicted Na—H bond length is 2.28797 Å, which is 0.041 Å shorter than the experimental value of 2.329 Å, while LDA predicts an even shorter distance of 2.23910 Å. As Li progressively replaces Na, the (Na/Li)-H bond contracts: 2.25632 Å at $x = 0.25$, 2.19367 Å at $x = 0.5$, and reaches a minimum of 2.05242 Å at $x = 1$ ($LiMgH_3$). This trend reflects the smaller ionic radius of Li^+ (1.52 Å) compared to Na^+ (1.86 Å), resulting in stronger Li—H interactions.

These interactions strengthen due to the reduced ionic radius of Li, leading to tighter hydrogen coordination and contributing to the denser hydrogen packing observed in Li-substituted phases. The Mg—H bonds show minimal variation across the substitution range. For $NaMgH_3$, the Mg—H1 bond is 1.96760 Å (GGA), slightly shorter than the experimental value of 1.9826 Å. At $x = 1$, this bond reduces marginally to 1.91505 Å, in close agreement with the reported 1.922 Å. These subtle changes suggest that Mg maintains a consistent role in hydrogen bonding, unlike the more sensitive (Na/Li)-H interactions. This highlights Mg's stable contribution to the hydrogen storage process, in contrast to the more dynamically changing (Na/Li)-H bonds.

Hydrogen-hydrogen (H—H) distances also contract with increasing Li content, indicating denser hydrogen packing. The shortest H—H

Table 9
Selected interatomic distances (Å) and angles (deg) in $Na_{1-x}Li_xMgH_3$ ($x = 0$, 0.25, 0.5, 0.625, 0.75, 1).

Alloys	*Atoms*	*This Work (DFT)*		Expt. data at 295 K [39]	GGA [33]
		GGA	*LDA*		
$NaMgH_3$	*Na-H1 (×3)*	2.28797	2.23910	2.329	2.302
(Pnma)	*Na-H1 (×3)*	2.44490	2.40970	2.519	2.472
	Na-H2 (×2)	2.29428	2.26000	2.342	2.326
	Na-H2 (×2)	2.62728	2.58500	2.679	2.640
	Na-H2 (×2)	2.67834	2.64012	2.735	2.701
	Mg-H1 (×2)	1.96760	1.93053	1.9826	1.976
	Mg-H2 (×2)	1.95767	1.93032	1.958	1.967
	Mg-H2 (×2)	1.96248	1.93235	1.971	1.968
	H1-H2 (×2)	2.73585	2.69533		2.755
	H1-H2 (×2)	2.75378	2.69912		2.764
	H1-H2 (×2)	2.80398	2.71429		2.813
	H1-H2 (×2)	2.80719	2.76715		2.821
	Mg-Na (×2)	3.17736	3.13439		3.203
	Mg-Na (×2)	3.26826	3.20808		3.281
	Mg-Na (×2)	3.31691	3.25554		3.332
	Mg-Na (×2)	3.44744	3.40052		3.473
	H1-Mg-H2 (×2)	88.6878°	88.4935°		
	H1-Mg-H2 (×2)	91.0349°	88.6567°		
	H1-Mg-H2 (×2)	91.4833°	89.3409°		
	H1-Na-H2 (×2)	65.3767°	64.4305°		
	H1-Na-H2 (×2)	67.6563°	67.7592°		
	H1-Na-H2 (×2)	68.3181°	68.5336°		
	(Na/Li)-H1 (×3)	2.25632	2.20691	2.255	
$Li_{0.25}Na_{0.75}MgH_3$	*(Na/Li)-H1 (×3)*	2.40879	2.33709	2.576	
(Pnma)	*(Na/Li)-H2 (×2)*	2.26163	2.22223	2.357	
	(Na/Li)-H2 (×2)	2.62461	2.58034	2.704	
	(Na/Li)-H2 (×2)	2.64777	2.58119	2.710	
	Mg-H1 (×2)	1.94490	1.93086	1.944	
	Mg-H2 (×2)	1.94511	1.94760	1.9820	
	Mg-H2 (×2)	1.98536	1.97621	1.987	
	H-H	2.67092–2.79264	2.64041–2.77127		
	H1-Mg-H2 (×2)	87.7889°	87.5779°		
	H1-Mg-H2 (×2)	89.6298°	93.4409°		
	H1-Mg-H2 (×2)	90.7765°	94.1376°		
	H1-(Na/Li)-H2 (×2)	68.8535°	69.2362°		
	H1-(Na/Li)-H2 (×2)	69.2805°	70.4026°		
	H1-(Na/Li)-H2 (×2)	79.4229°	79.4232°		
	(Na/Li)-H1 (×3)	2.19367	2.16330	2.244	
$Li_{0.5}Na_{0.5}MgH_3$	*(Na/Li)-H1 (×3)*	2.44200	2.38921	2.703	
(Pnma)	*(Na/Li)-H2 (×2)*	2.21622	2.18042	2.316	
	(Na/Li)-H2 (×2)	2.55136	2.49841	2.645	
	(Na/Li)-H2 (×2)	2.64545	2.60229	2.791	
	Mg-H1 (×2)	1.92716	1.90750	1.937	
	Mg-H2 (×2)	1.95352	1.91974	1.9823	
	Mg-H2 (×2)	1.99510	1.93735	2.001	
	H-H	2.68508–2.80979	2.67056–2.81463		
	H1-Mg-H2 (×2)	87.3992°	88.1845°		
	H1-Mg-H2 (×2)	89.0850°	92.0156°		
	H1-Mg-H2 (×2)	91.7642°	94.6850°		
	H1-(Na/Li)-H2 (×2)	64.1205°	64.3556°		
	H1-(Na/Li)-H2 (×2)	70.1719°	68.4867		
	H1-(Na/Li)-H2 (×2)	79.9687°	79.9144°		
	(Na/Li)-H (×3)	1.93877	1.95988		
$Li_{0.625}Na_{0.375}MgH_3$	*(Na/Li)-H (×3)*	2.07445	2.07072		
(R3c)	*Mg-H (×3)*	1.91926	1.90141		
	Mg-H (×3)	2.00051	2.01108		
	H-H	2.62691–3.06741	2.56810–2.95957		
	Mg-Li (×1)	2.84767	2.78187		
	Mg-Li (×3)	3.25843	3.22607		
	Mg-Na (×1)	3.18961	3.18961		
	H1-Mg-H2 (×2)	78.3010°	84.8644°		
	H1-Mg-H2 (×2)	94.1564°	97.5737°		
	H1-Mg-H2 (×2)	102.5525°	101.5796°		
	H1-(Na/Li)-H2 (×2)	77.8589°	78.6374°		
	H1-(Na/Li)-H2 (×2)	86.9958°	85.9160°		
	H1-(Na/Li)-H2 (×2)	104.9621°	105.5367°		
	(Na/Li)-H (×3)	1.92301	1.91020		
$Li_{0.75}Na_{0.25}MgH_3$	*(Na/Li)-H (×3)*	2.06277	2.02974		
(R3c)	*Mg-H (×3)*	1.94339	1.91064		
	Mg-H (×3)	2.04286	2.00788		

(*continued on next page*)

Table 9 (*continued*)

Alloys	Atoms	This Work (DFT)		Expt. data at 295 K [39]	GGA [33]
		GGA	LDA		
	H-H	2.61503–3.11694	2.44372–2.95796		
	Mg-Li (×1)	2.84218	2.77131		
	Mg-Li (×3)	3.28131	3.24823		
	Mg-Na (×1)	3.07529	3.01161		
	H1-Mg-H2 (×2)	78.3010°	78.8782°		
	H1-Mg-H2 (×2)	83.2574°	84.2921°		
	H1-Mg-H2 (×2)	104.3579°	103.9818°		
	H1-(Na/Li)-H2 (×2)	73.1850°	78.6692°		
	H1-(Na/Li)-H2 (×2)	85.1069°	86.7626°		
	H1-(Na/Li)-H2 (×2)	106.0119°	104.8710°		
	Li-H (×3)	1.89981	1.87606		1.934
$LiMgH_3$	*Li-H (×3)*	2.05242	2.02677		2.073
(R3c)	*Mg-H (×3)*	1.91505	1.89111		1.922
	Mg-H (×3)	2.00989	1.98477		2.008
	H1-H2 (×2)	2.55278	2.52088		2.576
	H1-H2 (×2)	2.67077	2.63739		2.691
	H1-H2 (×2)	2.79883	2.76385		2.846
	H1-H2 (×2)	2.97869	2.96237		2.966
	Mg-Li (×1)	2.79489	2.75997		2.794
	Mg-Li (×3)	2.89673	2.86064		2.919
	H1-Mg-H2 (×2)	78.8481°	78.8481°		
	H1-Mg-H2 (×2)	90.9407°	90.9407°		
	H1-Mg-H2 (×2)	102.1020°	102.1020°		
	H1-Li-H2 (×2)	76.9093°	76.9093°		
	H1-Li-H2 (×2)	90.4586°	90.4586°		
	H1-Li-H2 (×2)	104.2812°	104.2812°		

distance decreases from 2.73585 Å in $NaMgH_3$ to 2.57885 Å in $LiMgH_3$, closely matching experimental trends and supporting enhanced structural compactness due to Li substitution. This contraction in H—H distance is consistent with the expectation of increased hydrogen packing density, a critical factor in improving the material's hydrogen storage efficiency.

A structural phase transition is observed at $x = 0.625$, where the symmetry changes from orthorhombic ***Pnma*** to rhombohedral ***R3c***

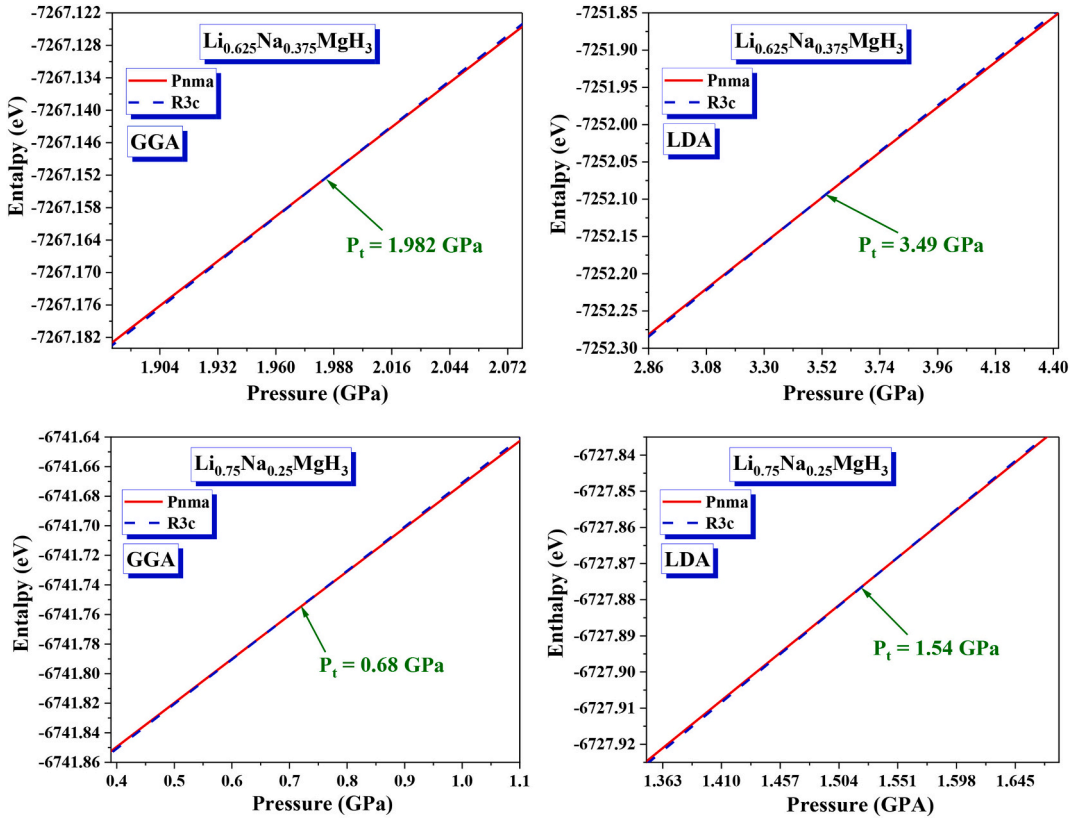

Fig. 9. Variation of total enthalpy as a function of pressure for the $Na_{1-x}Li_xMgH_3$ alloy at $x = 0.625$ and $x = 0.75$ in the ***Pnma*** and ***R3c*** phases, using GGA and LDA approximations.

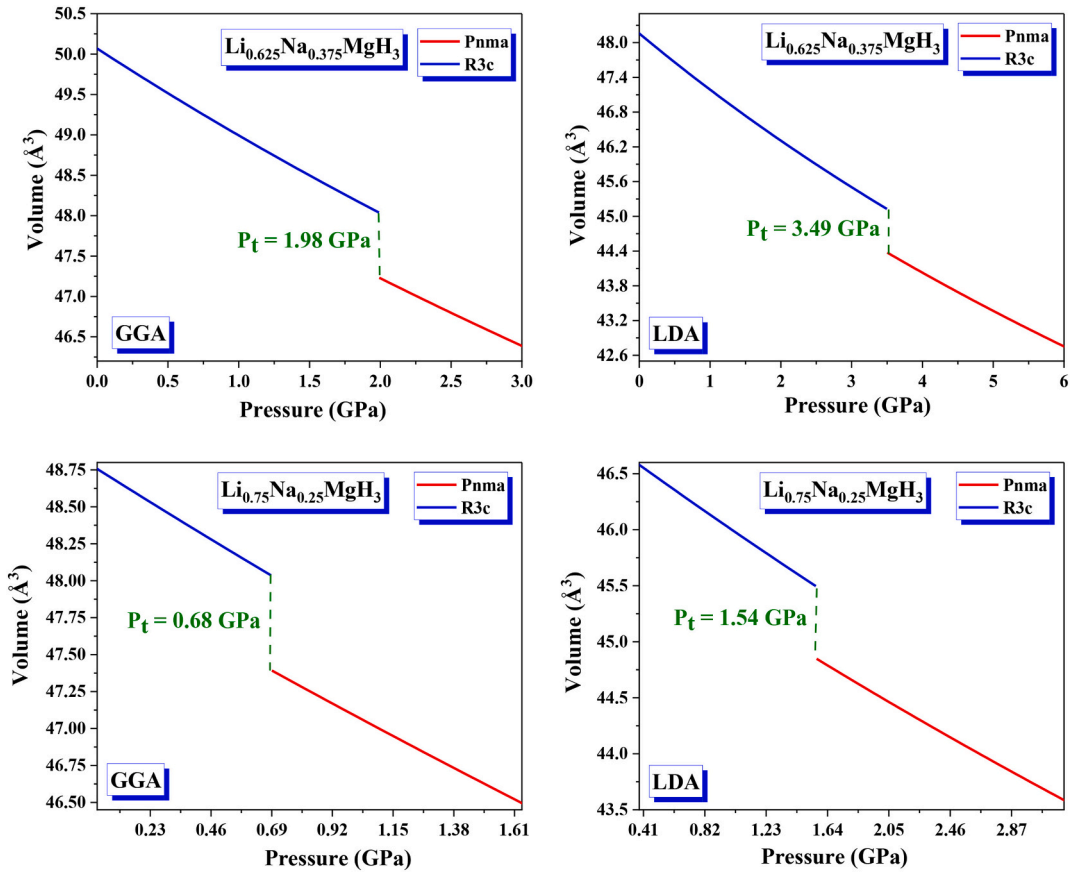

Fig. 10. Pressure-volume relationship for the unit cell of $Na_{1-x}Li_xMgH_3$ in the ***Pnma*** and ***R3c*** structures at $x = 0.625$ and $x = 0.75$, calculated using GGA and LDA approximations.

(Fig. 5). This transition is marked by a notable increase in bond angles. The H1-Mg-H2 angle, initially 91.0349° in $NaMgH_3$, remains stable up to $x = 0.5$ but increases to 94.1564° at $x = 0.625$ and further to 104.3579° at $x = 1$. The latter exceeds the experimental value of 102.102° by approximately 2.25°, emphasizing the angular distortion in the ***R3c*** phase. This angular distortion suggests a significant restructuring of the crystal lattice as the material transitions to a more densely packed and angularly distorted structure, especially at higher Li concentrations.

The observed increase in hydrogen desorption temperature with rising lithium content in $Na_{1-x}Li_xMgH_3$ is closely correlated with the structural modifications induced by Li substitution. Our analysis reveals a systematic contraction of (Na/Li)-H and H—H bond lengths and a significant increase in bond angles following the phase transition from orthorhombic (***Pnma***) to rhombohedral (***R3c***) symmetry at $x = 0.625$. These changes enhance hydrogen packing density and strengthen Li—H interactions, thereby requiring more energy for hydrogen release. These findings suggest that Li substitution leads to enhanced structural rigidity and hydrogen storage capacity, which aligns with the increased desorption temperatures observed in pathways (4) and (6). Conversely, the reduced enthalpy along pathways (2) and (4), which involve intermediate LiH and NaH phases, indicates more favorable dehydrogenation kinetics. Together, these results underscore the critical role of atomic-scale structural features in governing the hydrogen storage properties and thermal behavior of this class of complex hydrides.

3.7. Transitions pressure

To determine the most thermodynamically stable phase of a compound under pressure, the Gibbs free energy (G) is a key thermodynamic quantity. It is defined as [34]:

$$G = E_{tot} + PV - TS \tag{13}$$

where E_{tot} is the total energy of the system, P is the applied pressure, V is the volume, and S is the entropy. However, since our first-principles calculations are performed at absolute zero temperature (0 K), the entropy term "TS" becomes negligible and can be omitted. Therefore, the Gibbs energy simplifies to the enthalpy H [74]:

$$H = E_{\text{tot}} + PV \tag{14}$$

To determine the structural phase transition pressure, the enthalpy differences between the orthorhombic ***Pnma*** and rhombohedral ***R3c*** phases are calculated as a function of pressure. These enthalpy curves are generated using energy–volume data under both the GGA and LDA approximations. The pressure at which the enthalpy curves of the two phases intersect marks the phase transition point, indicating the pressure at which both phases become energetically degenerate. In Fig. 9, the transition pressure of $Na_{1-x}Li_xMgH_3$ decreases with increasing lithium content. For $x = 0.625$, the transition pressures are 1.98 GPa (GGA) and 3.49 GPa (LDA), while for $x = 0.75$, they drop to 0.68 GPa (GGA) and 1.54 GPa (LDA).

This trend can be attributed to the substitution of sodium with lithium, where lithium, due to its smaller atomic radius and lower mass, introduces lattice distortions. These distortions increase the system's structural flexibility, lowering the critical pressure required for phase transformation. The results in Fig. 10 complement this observation, showing the pressure-volume relationship for $Na_{1-x}Li_xMgH_3$ at $x = 0.625$ and $x = 0.75$ in the ***Pnma*** and ***R3c*** crystal structures, calculated using both GGA and LDA. The ***Pnma*** structure shows a sharp volume reduction with pressure, and the phase transition occurs at 1.98 GPa (GGA) and 3.49 GPa (LDA) for $x = 0.625$, while the ***R3c*** structure undergoes a more

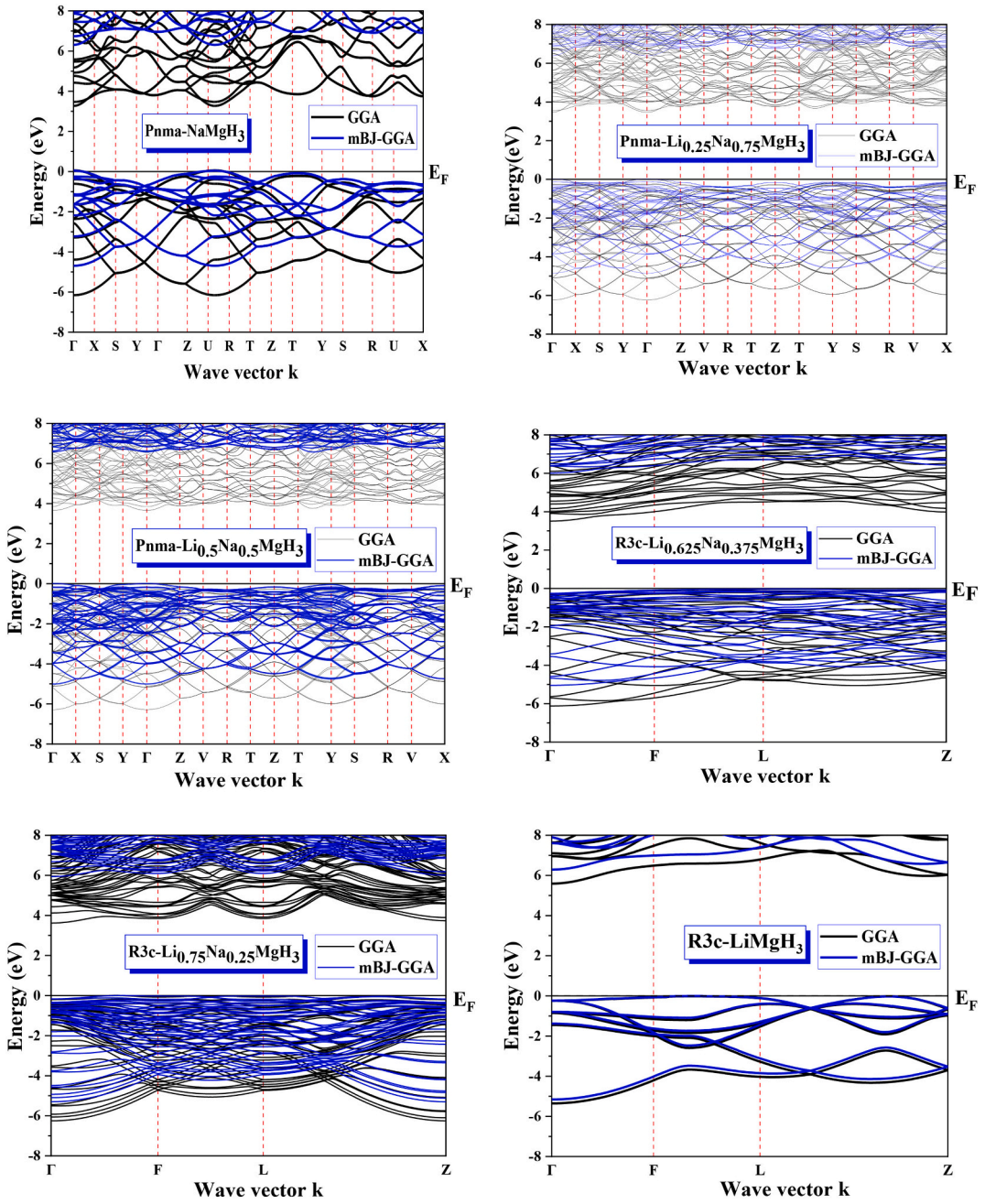

Fig. 11. Band structure along the high-symmetry paths of the *Brillouin* zone for the $Na_{1-x}Li_xMgH_3$ alloys at $x = 0$, 0.25, 0.5, 0.625, 0.75,1 calculated using GGA, and mBJ-GGA approximations.

gradual reduction in volume and transitions at higher pressures. For $x = 0.75$, the phase transition in the ***Pnma*** structure occurs at 0.68 GPa (GGA) and 1.54 GPa (LDA), confirming that increasing lithium content reduces the transition pressure. In contrast, the ***R3c*** structure transitions at slightly higher pressures.

The difference in phase transition behavior between the ***Pnma*** and ***R3c*** structures, combined with the observed decrease in transition pressure for increasing lithium content, highlights the impact of lithium substitution on the material's structural stability. The reduced transition pressure in the ***Pnma*** structure at higher lithium concentrations is particularly relevant in the context of hydrogen storage, where structural transformations that govern hydrogen release and uptake must occur at lower pressures for practical efficiency. Lower transition pressures indicate a more favorable thermodynamic pathway for hydrogen desorption, enhancing the material's utility in energy storage systems. These findings underscore the influence of lithium substitution on the mechanical properties and phase behavior of the material, with important implications for its use in applications requiring controlled structural transformations, such as in hydrogen storage. The smaller atomic size of lithium reduces the energy required for phase transition, enabling the material to undergo these transformations under more moderate pressure conditions.

3.8. *Electronic properties*

The electronic properties of $Na_{1-x}Li_xMgH_3$ alloys were analyzed to examine the effects of Li insertion on their physical characteristics. This study involved the calculation of band structures, bandgap energies (E_g), and the density of states (DOS) for various compositions of $Na_{1-x}Li_xMgH_3$ ($x = 0$, 0.25, 0.5, 0.625, 0.75, 1). Fig. 11 illustrates the band

Table 10
Calculated energy gap values using the GGA, LDA, mBJ-GGA, mBJ-LDA, and *Ev*-GGA approximations for $Na_{1-x}Li_xMgH_3$ ($x = 0$, 0.25, 0.5, 0.625, 0.75, 1) alloys in their most stable phases.

Alloys	E_g (eV)					
	GGA	*LDA*	*mBJ-GGA*	*mBJ-LDA*	*Ev-GGA*	*Exp. data*
$NaMgH_3$ (Pnma)	3.445, 3.45 [33], 3.52 [7]	3.429	6.436	6.767	5.263	3.5 [6]
$Li_{0.25}Na_{0.75}MgH_3$ (Pnma)	3.534, 3.67 [7]	3.511	6.438	6.713	5.055	
$Li_{0.5}Na_{0.5}MgH_3$ (Pnma)	3.696, 3.68 [7]	3.573	6.608	6.602	5.376	
$Li_{0.625}Na_{0.375}MgH_3$ (R3c)	3.590	3.538	6.068	6.227	5.125	
$Li_{0.75}Na_{0.25}MgH_3$ (R3c)	3.619, 3.71 [7]	3.548	5.938	6.158	5.498	
$LiMgH_3$ (R3c)	4.056, 3.98 [33], 4.15 [68]	3.988	6.447	6.679	5.754	

structures of the alloys, highlighting the results obtained using both GGA and mBJ-GGA functionals. In ***Pnma***-$NaMgH_3$, the valence band reaches its maximum and the conduction band reaches its minimum along the U–R direction, indicating the presence of an indirect band gap. In contrast, ***Pnma***-$Na_{0.25}Li_{0.75}MgH_3$ and ***Pnma***-$Na_{0.5}Li_{0.5}MgH_3$ exhibit direct band gaps, as both the valence band maximum (VBM) and the conduction band minimum (CBM) are located at the Γ point. For compositions adopting the ***R3c*** phase ($x = 0.625$, 0.75, and 1), the band gaps are again indirect. In these cases, the valence band maximum occurs along the high-symmetry directions L–Z, Γ–F, and F–L, respectively, while the conduction band minimum is consistently located at the Γ point for all three compositions.

Although slight variations in the exact band gap values are observed, the overall qualitative features of the band structures remain consistent across all compositions. This consistency reinforces the reliability of the computational methods and approximations employed in this study. The calculated band gap values (E_g) for each alloy, using the GGA, LDA, mBJ-GGA, mBJ-LDA, and *Ev*-GGA approximations, are presented in Table 10. The GGA results range from 3.445 eV to 4.056 eV, which are in close agreement with the theoretical value of 3.45 eV for $NaMgH_3$ reported by Vajeeston et al. [25]. Similarly, Xiao's group [7], using the VASP code within the GGA approximation, reported band gaps of 3.52, 3.67, 3.89, 3.68, and 3.71 eV for $Na_{1-x}Li_xMgH_3$ with x = 0, 0.25, 0.5 (I), 0.5 (II), and 0.75, respectively. These findings confirm that while GGA tends to underestimate the band gap compared to experimental data, it still offers a reasonable approximation. In comparison, the LDA approximation yields slightly lower values, ranging from 3.429 eV to 3.988 eV, reflecting its well-known tendency to underestimate band gaps even more significantly than GGA.

In contrast, the mBJ-GGA and mBJ-LDA methods predict significantly larger band gaps—6.436 to 6.447 eV and 6.679 to 6.767 eV, respectively due to the inclusion of more accurate exchange-correlation effects. The *Ev*-GGA method provides intermediate values, with calculated gaps between 5.263 eV and 5.754 eV, bridging the range between the conventional (GGA/LDA) and more advanced (mBJ) approximations. A noticeable trend is the widening of the band gap with increasing Li concentration, indicating that $Na_{1-x}Li_xMgH_3$ alloys become more insulating as x approaches 1. This behavior supports their potential application in high-resistivity materials such as insulators or semiconductors.

Theoretical calculations by Ghellab [74] also support this conclusion, showing that these compounds exhibit wide band gaps and insulating behavior in their density of states profiles. Weibin Z et al. combined machine learning with high-throughput DFT to predict the HSE band gap, CBM, and VBM of 2176 2D materials, identifying 766 potential $MoSi_2N_4$/2D heterostructures. This method reveals how structural changes, like unit cell reduction in $Na_{1-x}Li_xMgH_3$, affect electronic properties [75]. In $Na_{1-x}Li_xMgH_3$, increasing lithium content widens the band gap, enhancing electronic stability, reducing degradation, and improving hydrogen storage efficiency by promoting ionic interactions and increasing ionic conductivity.

Further insight into the electronic properties is provided by the partial density of states calculations for different Li concentrations, as shown in Fig. 12. The conduction bands are mainly influenced by Li/Na *s* and *p* states, while Mg *s* and *p* states contribute to both the valence and conduction bands. Additionally, H *s* states play a key role in the valence bands across all compositions. As Li content increases from 0 to 1, Fig. 12 reveals a growing contribution of Li *s* and *p* orbitals, while the Na *s* and *p* contribution decreases correspondingly. This shift in orbital contribution is consistent with the observed insulating behavior in the $Na_{1-x}Li_xMgH_3$ alloys for $x = 0$, 0.25, 0.5, 0.625, 0.75, and 1. Specifically, one of the three half-filled H *s* orbitals per formula unit is occupied by a metal atom (Li or Na), while the remaining two are filled by electrons from Mg. This complete filling of the valence band leads to the material's insulating character. The ***Pnma*** → ***R3c*** phase transition, occurring at $x = 0.625$, enhances the hydrogen storage properties by improving the electronic structure. The hydrogen gravimetric capacity increases from 6.00 wt% in $NaMgH_3$ ($x = 0$) to 7.50 wt% at $x = 0.625$, and 8.82 wt% at $x = 1$. This is linked to the more open and symmetric structure in the ***R3c*** phase, which facilitates hydrogen diffusion. The transition also reduces the electronic band gap from 3.445 eV in $NaMgH_3$ to 3.590 eV in $Li_{0.625}Na_{0.375}MgH_3$ (using the GGA approximation), weakening the hydrogen-metal bond and enabling easier desorption. These changes lead to lower desorption temperatures, better reversibility, and higher hydrogen storage capacity, making the ***R3c*** phase more suitable for practical hydrogen storage.

4. Conclusion

In this study, we conducted a comprehensive first-principles investigation of the structural, thermodynamic stability, electronic, and hydrogen storage properties of the $Na_{1-x}Li_xMgH_3$ ($x = 0$, 0.25, 0.5, 0.625, 0.75, 1) hydrides. Our results reveal that lithium substitution significantly enhances the hydrogen storage performance. The gravimetric hydrogen storage capacity increases from 6.00 wt% ($x = 0$) to 8.82 wt% ($x = 1$), and the volumetric capacity rises from 90 gH_2/l to 214 gH_2/l, surpassing the U.S. DOE targets. The theoretical specific capacity similarly improves from 1590 to 2331 mAh/g with increasing lithium content.

From a thermodynamic perspective, all four investigated dehydrogenation pathways are exothermic, with Pathway 4 exhibiting the most negative formation enthalpies (−79.43 to −104.30 kJ mol^{-1} H_2 using GGA), indicating it is the most stable route for hydride formation. However, this stability comes at the cost of high desorption temperatures (607–799 K), which may be less ideal for practical applications. In contrast, Pathway 7 demonstrates a more favorable balance between thermodynamic and kinetic properties for hydrogen release. The dehydrogenation enthalpy along this pathway decreases from −33.46 to −19.02 kJ mol^{-1} H_2 as lithium content increases, corresponding to a decline in desorption temperature from 256 K to 145 K. These values make Pathway 7 particularly attractive for low-temperature hydrogen desorption, especially in Li-rich compositions. Therefore, while Pathway 4 ensures robust compound stability, Pathway 7 emerges as the most efficient and practical for real-world hydrogen release, especially in systems requiring moderate temperature operation.

Additionally, binding and cohesive energy analyses show enhanced stability and tunable hydrogen-metal interactions with lithium substitution. A composition-induced phase transition from the orthorhombic ***Pnma*** to the trigonal ***R3c*** structure at $x = 0.625$ improves structural compactness and hydrogen packing. The electronic properties reveal that all compositions are wide-gap insulators, with the band gap

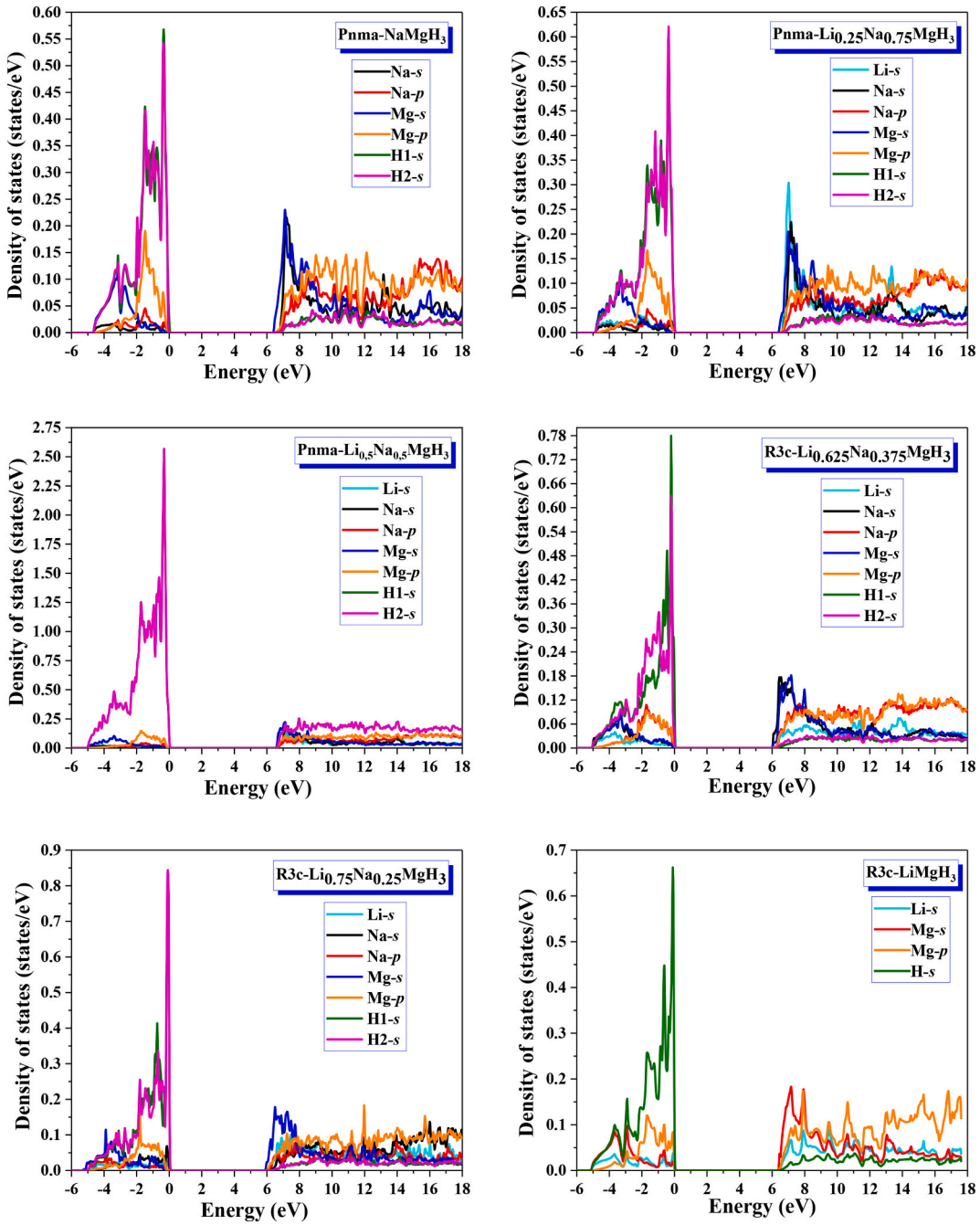

Fig. 12. The calculated partial density of states for $Na_{1-x}Li_xMgH_3$ ($x = 0$, 0.25, 0.5, 0.625, 0.75, 1) alloys in the most stable phase with the mBJ-GGA approximation.

increasing from 3.45 eV to 4.05 eV (GGA) and up to 6.77 eV (mBJ-LDA) as x increases, consistent with enhanced electronic stability in Li-rich phases. $Na_{1-x}Li_xMgH_3$ hydrides, particularly those with higher lithium content, offer a promising combination of high hydrogen storage capacity, favorable thermodynamic behavior, and structural and electronic tunability. These characteristics underscore their potential as next-generation materials for solid-state hydrogen storage technologies.

CRediT authorship contribution statement

S. Saadoun: Writing – review & editing, Writing – original draft, Software, Investigation, Formal analysis, Data curation, Conceptualization. **T. Ghellab:** Writing – original draft, Supervision, Software, Formal analysis, Data curation, Conceptualization. **H. Baaziz:** Validation, Software, Methodology, Investigation, Formal analysis, Conceptualization. **Z. Charifi:** Writing – review & editing, Software, Methodology, Investigation, Data curation.

Declaration of competing interest

The authors declare that they have no known competing financial interests or personal relationships that could have appeared to influence the work reported in this paper.

Data availability

Data will be made available on request.

References

[1] El M. Akkel, H. Ez-Zahraouy, Novel double hydride perovskites $Li_2TiF_{6-x}H_x$ as efficient materials for solid-state hydrogen storage: DFT insights, Int. J. Hydrog. Energy 101 (2025) 1406–1420, https://doi.org/10.1016/j.ijhydene.2025.01.023.

[2] B. Ahmed, M.B. Tahir, A. Ali, M. Sagir, DFT insights on structural, electronic, optical and mechanical properties of double perovskites X_2FeH_6 (X = ca and Sr) for hydrogen-storage applications, Int. J. Hydrog. Energy 50 (2024) 316–323, https://doi.org/10.1016/J.IJHYDENE.2023.10.237.

[3] G.M. Mustafa, et al., Study of structural, optical, mechanical, thermoelectric, and hydrogen storage properties of $CsXH_3$ (X = Ca, Sr, Ba) hydrides, Int. J. Hydrog. Energy 92 (2024) 938–948, https://doi.org/10.1016/J.IJHYDENE.2024.10.245.

[4] W.S. Chai, Y. Bao, P. Jin, G. Tang, L. Zhou, A review on ammonia, ammonia-hydrogen and ammonia-methane fuels, Renew. Sust. Energ. Rev. (2021), https://doi.org/10.1016/j.rser.2021.111254.

[5] W. Liu, et al., Trends and future challenges in hydrogen production and storage research, Environ. Sci. Pollut. Res. (2020), https://doi.org/10.1007/s11356-020-09470-0.

[6] L. Schlapbach, A. Züttel, Hydrogen-storage materials for mobile applications, Nature 474 (2002) 353–358.

[7] X.B. Xiao, B.Y. Tang, S.Q. Liao, L.M. Peng, W. jiang Ding, Thermodynamic and electronic properties of quaternary hydrides $Li_xNa_{1-x}MgH_3$, J. Alloys Compd. 474 (1–2) (Apr. 2009) 522–526, https://doi.org/10.1016/j.jallcom.2008.06.127.

[8] R. Chami, A. Lekdadri, M. Baaddi, M. Chafi, First-principles insight of hydrogen storage properties of mixed perovskite hydrides $Na_{1-x}K_xMgH_3$ x<0.75, Bull. Mater. Sci. (2023), https://doi.org/10.1007/s12034-023-03035-wS.

[9] N. Klopčič, I. Grimmer, F. Winkler, M. Sartory, A. Trattner, A review on metal hydride materials for hydrogen storage, J Energy Storage 72 (2023) 108456, https://doi.org/10.1016/J.EST.2023.108456.

[10] S. Cheng, X. Cheng, M.H. Tahir, Z. Wang, J. Zhang, Synthesis of rice husk activated carbon by fermentation osmotic activation method for hydrogen storage at room temperature, Int. J. Hydrog. Energy 62 (2024) 443–450, https://doi.org/10.1016/J.IJHYDENE.2024.03.092.

[11] S.R. Parida, M. Amrutha, S. Sahu, B. Chakraborty, Density functional theory and ab initio molecular dynamics calculations for reversible hydrogen storage in yttrium-decorated azatriphenylene COF, Fuel 403 (2026), https://doi.org/10.1016/j.fuel.2025.136061.

[12] J. Gao, Y. Pan, I.P. Jain, F. Yang, J. Zhu, Exploring the structure, hydrogen storage capacity and hydrogen storage mechanism of $X_3N_3H_6$ hydrides for hydrogen storage, Appl. Mater. Today 44 (2025) 102755, https://doi.org/10.1016/J.APMT.2025.102755.

[13] Y. Pan, Y. Zhu, Theoretical prediction of novel phase, phonon dynamics and physical properties of $KAlH_4$ hydride for hydrogen storage, Int. J. Hydrog. Energy 131 (2025) 221–228, https://doi.org/10.1016/j.ijhydene.2025.04.422.

[14] Y. Zhu, Y. Pan, F. Yang, J. Zhu, Investigation of structure, dehydrogenated behavior, mechanical and physical properties of $LiAlH_4$ hydrogen storage material, Int. J. Hydrog. Energy 136 (2025) 11–20, https://doi.org/10.1016/j.ijhydene.2025.05.053.

[15] K. Ikeda, T. Sato, S.I. Orimo, Perovskite-type hydrides - synthesis, structures and properties, Int. J. Mater. Res. 99 (5) (2008) 471–479, https://doi.org/10.3139/146.101671.

[16] J. Bellosta von Colbe, et al., Application of hydrides in hydrogen storage and compression: Achievements, outlook and perspectives, Int. J. Hydrog. Energy 44 (15) (2019) 7780–7808, https://doi.org/10.1016/j.ijhydene.2019.01.104.

[17] H. Wu, W. Zhou, T.J. Udovic, J.J. Rush, T. Yildirim, Crystal chemistry of perovskite-type hydride $NaMgH_3$: Implications for hydrogen storage, Chem. Mater. 20 (6) (2008) 2335–2342, https://doi.org/10.1021/cm703356v.

[18] W. Azeem, et al., Computational insights of double perovskite X_2CaCdH_6 (X = Rb and Cs) hydride materials for hydrogen storage applications: A DFT analysis, Int. J. Hydrog. Energy 79 (2024) 514–524, https://doi.org/10.1016/J.IJHYDENE.2024.07.044.

[19] T. Ghellab, et al., The elastic, mechanical, and thermodynamic properties of $NaXH_4$ (X = B, Al) intended for the storage of hydrogen: An ab-initio study, Phys. B Condens. Matter 638 (2022) 413851, https://doi.org/10.1016/J.PHYSB.2022.413851.

[20] Z.M. Wang, J.J. Li, S. Tao, J.Q. Deng, H. Zhou, Q. Yao, Structure, thermal analysis and dehydriding kinetic properties of $Na_{1-x}Li_xMgH_3$ hydrides, J. Alloys Compd. 660 (2016) 402–406, https://doi.org/10.1016/j.jallcom.2015.11.127.

[21] T. Tang, Y. Tang, First-principles investigations for the structural, optoelectronic and hydrogen storage properties of double perovskite $KNaMg_2F_{6-x}H_x$ and $KNaAe_2H_6$(ae=be, Mg, ca), Int. J. Hydrog. Energy 61 (2024) 13–24, https://doi.org/10.1016/j.ijhydene.2024.02.237.

[22] K. Ikeda, Y. Kogure, Y. Nakamori, S. Orimo, Reversible hydriding and dehydriding reactions of perovskite-type hydride $NaMgH_3$, Scr. Mater. 53 (3) (2005) 319–322, https://doi.org/10.1016/j.scriptamat.2005.04.010.

[23] Y. Pan, J. Gao, Exploring the hydrogen storage capacity, dehydrogenated mechanism, electronic and optical properties of $AMMgH_3$ hydrides for hydrogen storage, J Energy Storage 124 (2025) 116869, https://doi.org/10.1016/J.EST.2025.116869.

[24] S. Lesz, B. Hrapkowicz, M. Karolus, K. Gołombek, Characteristics of the Mg-Zn-ca-Gd alloy after mechanical alloying, Materials 14 (1) (2021) 1–14, https://doi.org/10.3390/ma14010226.

[25] D. Kumar, R.K. Phanden, L. Thakur, "A review on environment friendly and lightweight Magnesium-Based metal matrix composites and alloys," in *Materials Today: Proceedings*, Elsevier Ltd (2020) 359–364, https://doi.org/10.1016/j.matpr.2020.07.424.

[26] M. Pęska, T. Czujko, M. Polański, Hydrogenation ability of Mg-Li alloys, Energies 13 (8) (2020), https://doi.org/10.3390/en13082080.

[27] J. Liu, Q. Yuan, W. Huang, X. Song, A novel nanoporous Mg-Li material for efficient hydrogen generation, Journal of Magnesium and Alloys 10 (11) (2022) 3054–3063, https://doi.org/10.1016/J.JMA.2021.09.022.

[28] Y. Pan, J. Gao, Transition metal improved the dehydrogenated capacity, electronic and optical properties of the layered V_2C MXene for hydrogen evolution reaction, Surf Interfaces 62 (2025), https://doi.org/10.1016/j.surfin.2025.106185.

[29] E. Boateng, A.R. Thiruppathi, C.K. Hung, D. Chow, D. Sridhar, A. Chen, Functionalization of graphene-based nanomaterials for energy and hydrogen storage, Electrochim. Acta 452 (2023) 142340, https://doi.org/10.1016/J.ELECTACTA.2023.142340.

[30] F. Yang, Y. Pan, I.P. Jain, Single atom enhanced the catalytic activity of borophene catalysts for hydrogen evolution reaction, Int. J. Hydrog. Energy 140 (2025) 223–232, https://doi.org/10.1016/j.ijhydene.2025.05.339.

[31] F. Cheng, Z. Tao, J. Liang, J. Chen, Efficient hydrogen storage with the combination of lightweight Mg/MgH_2 and nanostructures, Chem. Commun. 48 (59) (2012) 7334–7343, https://doi.org/10.1039/c2cc30740e.

[32] K. Ikeda, Y. Kogure, Y. Nakamori, S. Orimo, Formation region and hydrogen storage abilities of perovskite-type hydrides, Prog. Solid State Chem. (2007), https://doi.org/10.1016/j.progsolidstchem.2007.01.005.

[33] P. Vajeeston, P. Ravindran, A. Kjekshus, H. Fjellvåg, First-principles investigations of the $MMgH_3$ (M = Li, Na, K, Rb, Cs) series, J. Alloys Compd. 450 (1–2) (2008) 327–337, https://doi.org/10.1016/j.jallcom.2006.10.163.

[34] S. Al, C. Kurkcu, C. Yamcicier, High pressure phase transitions and physical properties of Li2MgH4; implications for hydrogen storage, Int. J. Hydrog. Energy 45 (7) (2020) 4720–4730, https://doi.org/10.1016/j.ijhydene.2019.12.005.

[35] B. Pfrommer, C. Elsasser, M. Fahnle, Possibility of Li-Mg and Al-Mg hydrides being metallic, Phys. Rev. B 50 (1994) 5089.

[36] S. Tao, Z.M. Wang, J.J. Li, J.Q. Deng, H. Zhou, Q.R. Yao, Improved dehydriding properties of $NaMgH_3$ perovskite hydride by addition of graphitic carbon nitride, Mater. Sci. Forum (2016) 502–508, https://doi.org/10.4028/www.scientific.net/MSF.852.502.

[37] K. Ikeda, Y. Nakamori, S. Orimo, Formation ability of the perovskite-type structure in $Li_xNa_{1-x}MgH_3$ (x = 0, 0.5 and 1.0), Acta Mater. 53 (12) (2005) 3453–3457, https://doi.org/10.1016/j.actamat.2005.04.001.

[38] L.F. Contreras Vasquez, Y. Liu, C. Paterakis, D. Reed, D. Book, Hydrogen sorption properties of $Li_xNa_{1-x}MgH_3$ (x = 0, 0.2, 0.5 & 0.8), Int. J. Hydrog. Energy 42 (35) (2017) 22589–22597, https://doi.org/10.1016/j.ijhydene.2017.03.041.

[39] R. Martínez-Coronado, J. Sánchez-Benítez, M. Retuerto, M.T. Fernández-Díaz, J. A. Alonso, High-pressure synthesis of $Na_{1-x}Li_xMgH_3$ perovskite hydrides, J. Alloys Compd. 522 (2012) 101–105, https://doi.org/10.1016/j.jallcom.2012.01.097.

[40] P. Blaha, K. Schwarz, P. Sorantin, S.B. Trickey, Full-potential, linearized augmented plane wave programs for crystalline systems, Comput. Phys. Commun. (1990).

[41] I.E. Gaa, P. Hohenbergt Ecole, X. Superzeure, I'aris and W. Konnt, Phys. Rev. 136 (1965) B864.

[42] M. Achqraoui, M. El Akkel, N. Bekkioui, H. Ez-Zahraouy, First principles calculation of perovskite-type hydrides KXH_3 (X=Al, Cu) for hydrogen storage applications, E3S Web Conf. (2023), https://doi.org/10.1051/e3sconf/202346900067.

[43] J.P. Perdew, K. Burke, M. Ernzerhof, Generalized gradient approximation made simple, Phys. Rev. Lett. 77 (1996) 3865.

[44] E. Engel, S.H.V., Exact exchange-only potentials and the virtial relatioon as microscopic criteria for generelazed gradient approximations, Phys. Rev. B 47 (1993) 13164.

[45] A.D. Becke, E.R. Johnson, A simple effective potential for exchange, J. Chem. Phys. 124 (22) (2006), https://doi.org/10.1063/1.2213970.

[46] B.F.D. Murnaghan, The Compressibility of Media under Extreme Pressures, Texas Public, 1915.

[47] D. N., K. K., A. R., B. B., Ewa Ronnebro, Investigation of the perovskite related structures of $NaMgH_3$, $NaMgF_3$ and Na AlH_3 6, Alloys Compd. 299 (2000) 101–106.

[48] X. Xiao, et al., Performance of $LiTaO_3$ crystals and thin films and their application, Crystals 13 (2023), https://doi.org/10.3390/cryst13081233.

[49] O. Hakami, H.J. Alathlawi, Study of mechanical, optoelectronic, and thermoelectric characteristics of be/M g ions based double perovskites A_2FeH_6 (a= be, Mg) for hydrogen storage applications, Int. J. Hydrog. Energy 83 (2024) 307–316, https://doi.org/10.1016/J.IJHYDENE.2024.08.143.

[50] H. Khenfer, et al., Bonding effects for hydrogen storage improvement in Li-based hydrides, Mater Today Commun 27 (2021), https://doi.org/10.1016/j.mtcomm.2021.102400.

[51] P. Pluengphon, P. Tsuppayakorn-aek, W. Sukmas, B. Inceesungvorn, T. Bovornratanaraks, Dynamical stabilization and H-vacancy diffusion kinetics of lightweight complex hydrides: Ab initio study for hydrogen storage improvement, Int. J. Hydrog. Energy 46 (43) (2021) 22591–22598, https://doi.org/10.1016/j.ijhydene.2021.04.070.

[52] N. Al-Zoubi, A. Almahmoud, A. Almahmoud, A. Obeidat, Theoretical assessment of a novel $NaXH_3$ and KXH_3 (X = Tc, Ru and Rh) perovskite hydrides for hydrogen storage, Int. J. Hydrog. Energy 93 (2024) 822–831, https://doi.org/10.1016/j.ijhydene.2024.11.020.

[53] A. Almahmoud, H. Alkhalidi, A. Obeidat, Comprehensive DFT Analysis of Structural, Mechanical, Electronic, Optical, and Hydrogen Storage Properties of Novel Perovskite-Type Hydrides Y_2CoH_8 (Y= Ca, Ba, Mg, Sr) [Online]. Available, https://ssrn.com/abstract=5012785, 2025.

[54] A. Almahmoud, H. Alkhalidi, A. Obeidat, First-Principles Investigation of Hydrogen Storage in Novel X_2FeH_5 Hydrides (X = Ca, Mg, Ba) [Online]. Available, https://ssrn.com/abstract=5034496, 2025.
[55] A. Obeidat, H. Alkhalidi, A. Almahmoud, A. Jaradat, Structural, electronic, mechanical, dynamical, and optical properties of KX_3H_8 (X = Sc, V, and Cr) hydrides: A DFT perspective [Online]. Available, https://ssrn.com/abstract=5208670, 2025.
[56] A. Obeidat, A. Almahmoud, H. Alkhalidi, M. Gharaibeh, First-principles examination of the structural, hydrogen storage, mechanical, electronic, and optical properties of $K_2BAl_{1-x}Ga_xH_6$ (B=Li, Na; x = 0, 0.25, 0.5, 0.75, 1) double perovskite hydrides, Int. J. Hydrog. Energy 153 (2025), https://doi.org/10.1016/j.ijhydene.2025.150286.
[57] H. Alkhalidi, A. Almahmoud, A. Obeidat, Theoretical Investigation of Double Perovskite Hydrides X_2CaAlH_6 (X = K, Rb, and Cs) for Hydrogen Storage Applications [Online]. Available, https://ssrn.com/abstract=5134289, 2025.
[58] S.V. Alapati, J.K. Johnson, D.S. Sholl, Identification of destabilized metal hydrides for hydrogen storage using first principles calculations, J. Phys. Chem. B 110 (17) (2006) 8769–8776, https://doi.org/10.1021/jp060482m.
[59] S. Karfaf, B. Bennecer, G. Uur, Uur, Phase transitions and lattice dynamics in perovskite-type hydride $Li_xNa_{1-x}MgH_3$, J. Phys. Condens. Matter 31 (50) (2019), https://doi.org/10.1088/1361-648X/ab3cfe.
[60] Y. Pan, Z. Yang, H. Zhang, Investigating the structural, mechanical, elastic anisotropy and thermodynamic properties of ta-C ultrahigh temperature ceramics via first-principles calculations, Ceram. Int. 51 (8) (2025) 10660–10669, https://doi.org/10.1016/j.ceramint.2024.12.497.
[61] Y. Pan, lirong Xu, New insight into the structural, mechanical and thermodynamic properties of Mo_2C MXene as the ultrahigh temperature ceramics, Mater. Today Chem. 42 (2024), https://doi.org/10.1016/j.mtchem.2024.102449.
[62] Y. Pan, Y. Zhu, New insight into the structural, hydrogen storage capacity, dehydrogenated mechanism and physical properties of alkali metal $AMAlH_4$ hydrides, J. Alloys Compd. 1021 (2025), https://doi.org/10.1016/j.jallcom.2025.179661.
[63] Y. Pan, M. Wen, Ab-initio calculations of mechanical and thermodynamic properties of TM (transition metal: 3d and 4d)-doped Pt_3Al, Vacuum 156 (2018) 419–426, https://doi.org/10.1016/j.vacuum.2018.08.010.
[64] D.A. Sheppard, M. Paskevicius, C.E. Buckley, Thermodynamics of hydrogen desorption from $NaMgH_3$ and its application as a solar heat storage medium, Chem. Mater. 23 (19) (2011) 4298–4300, https://doi.org/10.1021/cm202056s.
[65] K. Ikeda, et al., Thermodynamical stability and electronic structure of a perovskite-type hydride, $NaMgH_3$, J. Alloys Compd. 446–447 (2007) 162–165, https://doi.org/10.1016/j.jallcom.2007.03.093.
[66] N. Bouri, T.A. Geleta, K.W. Guji, D. Behera, K. Nouneh, Numerical analysis of photovoltaic performance in $NaSnCl_3$ and $KSnCl_3$ perovskite absorber layers for solar energy harvesting: SCAPS-1D study, Mater Today Commun 40 (2024), https://doi.org/10.1016/j.mtcomm.2024.110014.
[67] T. Ghellab, Z. Charifi, H. Baaziz, Uğur Uğur, G. Uğur, F. Soyalp, First principles study of hydrogen storage material $NaBH_4$ and $LiAlH_4$ compounds: Electronic structure and optical properties, Phys Scr 91 (4) (2016), https://doi.org/10.1088/0031-8949/91/4/045804.
[68] G.B. Skinner, R.C. Sweet, S.K. Davis, Davis, Shock tube experiments on the pyrolysis of deuterium-substituted ethylenes, J. Phys. Chem. 75 (1) (1971) 1–12.
[69] A. Züttel, P. Wenger, S. Rentsch, P. Sudan, P. Mauron, C. Emmenegger, $LiBH_4$ a new hydrogen storage material, J. Power Sources (2003) 1–7, https://doi.org/10.1016/S0378-7753(03)00054-5.
[70] K. Sathupun, T. Bovornratanaraks, P. Pluengphon, Ni-induced photoabsorption and hydrogen desorption on the Li-Mg hydrides using ab initio calculation, Solid State Commun. 347 (2022) 114736, https://doi.org/10.1016/j.ssc.2022.114736.
[71] B. Ahmed, M. Bilal Tahir, M. Sagir, A. Parveen, Z. Abbas, A.A. Nassani, First-principles study of Ti-based X_2TiH_5 (X = Mg, ca, Sr) hydrides for advanced hydrogen storage applications, Chem. Phys. 589 (2025), https://doi.org/10.1016/j.chemphys.2024.112499.
[72] A. Bouamrane, J.P. Laval, J.P. Soulie, J.P. Bastide, Structural characterization of $NaMgH_2F$ and $NaMgH_3$, Mater. Res. Bull. 35 (4) (2000) 545–549, https://doi.org/10.1016/S0025-5408(00)00249-X.
[73] D. Li, T. Zhang, S. Yang, Z. Tao, J. Chen, Ab initio investigation of structures, electronic and thermodynamic properties for Li-Mg-H ternary system, J. Alloys Compd. 509 (32) (2011) 8228–8234, https://doi.org/10.1016/j.jallcom.2011.05.084.
[74] T. Ghellab, Z. Charifi, H. Baaziz, K. Bouferrache, B. Hamad, Electronic structure and optical properties of complex hydrides $LiBH_4$ and $NaAlH_4$ compounds, Int. J. Energy Res. 43 (8) (2019) 3653–3667, https://doi.org/10.1002/er.4517.
[75] W. Zhang, J. Guo, Lv. X, F. Zhang, Combined machine learning and high-throughput calculations predict Heyd-Scuseria-Ernzerhof band gap of 2D materials and potential $MoSi_2N_4$ heterostructures, Phys. Chem. Lett. 15 (20) (2024) 5413–541923, https://doi.org/10.1021/acs.jpclett.4c01013.